
Article:
Ng, F.S.L. orcid.org/0000-0001-6352-0351 and Hughes, A.L.C. (2018) Reconstructing ice-flow fields from streamlined subglacial bedforms: a kriging approach. Earth Surface Processes and Landforms. ISSN 0197-9337

https://doi.org/10.1002/esp.4538

Earth Surface Processes and Landforms
BSG British Society for Geomorphology

Reconstructing ice-flow fields from streamlined subglacial bedforms: a kriging approach

Journal:	*Earth Surface Processes and Landforms*
Manuscript ID	ESP-18-0292.R1
Wiley - Manuscript type:	Research Article
Date Submitted by the Author:	n/a
Complete List of Authors:	Ng, Felix; University of Sheffield, Department of Geography Hughes, Anna; University of Bergen and Bjerknes Center for Climate Research, Department of Earth Science
Keywords:	glacial reconstruction, palaeoglaciology, kriging, subglacial bedforms, ice stream

Reconstructing ice-flow fields from streamlined subglacial bedforms: a kriging approach

Felix S. L. Ng[1*] and Anna L. C. Hughes[2]

[1]Department of Geography, University of Sheffield, Sheffield S10 2TN, UK

[2]Department of Earth Science, University of Bergen and Bjerknes Centre for Climate Research, N-5020 Bergen, Norway

*Corresponding author

Abstract

The orientation of several landforms, e.g. drumlins, flutes, crag-and-tails, and mega-scale glacial lineations, records the direction of the overlying ice flow that created them. Populations of such features are used routinely to infer former ice-flow patterns, which serve as the building blocks of reconstructions of palaeo ice-sheet evolution. Currently, the conceptualisation of flow patterns from these flow-direction records is done manually and qualitatively, so the extractable glaciological information is limited. We describe a kriging method (with MATLAB code implementation) that calculates continuous fields of ice-flow direction, convergence, and curvature from the flow-direction records, and which yields quantitative results with uncertainty estimates. We test the method by application to the subglacial bedforms of the Tweed Valley Basin, UK. The results quantify the convergent flow pattern of the Tweed palaeo-Ice Stream in detail and pinpoint its former lateral shear margins and where ice flowed around basal bumps. Ice-flow parameters retrieved by this method can enrich ice-sheet reconstructions and investigations of subglacial till processes and bedform genesis.

1. Introduction

The flow patterns of ice sheets and glaciers evolve as their geometry, flow mechanics (i.e., internal deformation and basal sliding) and thermal regime adjust under the influence of external conditions, e.g. changing climate. In studies of past glaciation, reconstructing ice-flow patterns is an exercise that yields vital information about an ice mass's history of growth, decay and potentially complex dynamics. One method of reconstruction uses physically-based glaciological models to simulate the ice motion and hindcast the flow field numerically (e.g. Tarasov and Peltier, 1999; Marshall et al., 2000; Hubbard et al., 2009). A second method infers ice-flow patterns from their geomorphological record by interpreting spatial assemblages of streamlined features whose orientation indicates the direction of palaeo ice flow, e.g. subglacial bedforms such as drumlins, crag-and-tails, and mega-scale glacial lineations (MSGLs) (Kleman and Borgström, 1996; Clark, 1997; Kleman et al., 2006). Patterns interpreted from such evidence of former ice-flow directions are increasingly used to constrain the first method (e.g. Li et al., 2007; Patton et al., 2017).

Here we contribute to the second method (geomorphological inversion) by providing a quantitative tool for estimating the palaeo ice-flow field from measurements of flow directions preserved across a deglaciated land surface. We reserve the term "flow field" for describing the geometric pattern excluding flow speed, and write "velocity field" where speed is also included. The flow-direction measurements are derived from mapping of streamlined bedforms identified either in the field, or from aerial photos, satellite imagery and/or digital elevation models (DEMs). Often, each landform is mapped as a lineament along its crestline (Figure 1a), with start and end points depicting the palaeo ice-flow direction (as opposed to orientation, which is ambiguous by 180°) inferred from the bedform's shape and context (e.g. Greenwood

and Clark, 2009). In some studies, the outline of the bedform is mapped in addition to its crestline (e.g. Rose and Letzer, 1977). Where only the outline has been mapped (e.g. Hughes et al., 2010), this can be converted to a lineament (e.g. using its longest internal transect as a proxy, as in Spagnolo et al., 2010; 2011). Each lineament's azimuth and midpoint position constitute observational data. A collection of mapped lineaments and/or outlines interpreted to record the same ice-flow event, based on the assumption that similarity of bedform characteristics (e.g. length, direction, spacing) indicates contemporaneous generation, is termed a flowset (Figure 1b) (e.g. Greenwood and Clark, 2009). The practitioner visualises the flowset as a whole to conceptualise the palaeo-flow field by sketching flowlines or (more crudely) an array of arrows summarising the palaeo ice flow (Figure 1c). A final, additional stage of interpretation occurs when the relationships between the reconstructed flow patterns of multiple flowsets, together with information about their relative timing, are analysed to piece together the regional ice-flow history and gauge the location of former ice divides. Examples of this procedure appear in the reconstructions of the Late-Weichselian Laurentide, Scandinavian, Barents Sea, and British ice sheets by Clark et al. (2000), Kleman et al. (1997), Winsborrow et al. (2010) and Hughes et al. (2014), respectively.

We focus on the step that conceptualises the ice-flow field for a given flowset, which relies on human perception and does not lend itself to quantitative uncertainty estimates. For the same flowset, different practitioners may reconstruct flow fields with different smoothness and detail depending on how much respect they pay to local variability across individual lineaments. In those parts of a flowset sparse or lacking in bedforms, discordance between reconstructions is more likely. Subjectivity extends also to the areal limit of the flow field that the practitioner perceives as reconstructable from

a flowset. Because the flow-direction measurements are quantitative, it seems that more robust results could be gained from them.

As introduced further in Section 2, by "flow field" we mean ice-flow direction as a mathematical function of position. Estimating this field from a finite set of observations is a spatial interpolation problem, and a quantitative approach is desirable for several reasons: (1) It allows palaeo flowlines (Figure 1d) to be traced through the field at any spatial density, unlimited by those selective flowlines drawn by the practitioner in the existing approach. (2) Equipped with uncertainty estimates, the reconstructed flow field can more reliably and usefully inform the glacial history reconstruction. (3) The reconstructed flow field can be computed on any spatial grid/mesh system for precise and comprehensive comparison with palaeo-flow fields simulated by numerical glaciological models. (4) The reconstructed field facilitates exploration of diverse aspects of ice-flow dynamics, such as a comparison of the structural features of modern and palaeo ice-flow fields (the former deriving from the present-day Antarctic and Greenland Ice Sheets). (5) Reconstructed ice-flow directions enable new geospatial analyses where they are compared or correlated against independent geomorphic or sedimentological attributes (e.g. till fabrics), or where they are studied alongside morphometric data of bedforms to elucidate their origin. We elaborate on some of these topics in Section 5.

Over the past two decades, glacial geomorphological inversion attempts have conceptualised ice-flow events by using the qualitative approach, and despite developments to attach glaciological significance to flowsets (Stokes and Clark, 1999; Greenwood and Clark, 2009), a numerical method for interpolating flow fields from bedform-directional data has not been forthcoming. The vast improvements in the quality and amount of Earth-Observation data have facilitated the detection and

mapping of bedforms in increasing numbers and detail, and motivated algorithms for their automated mapping (Saha et al., 2011; Maclachlan and Eyles, 2013), but not for quantitative reconstruction of ice flow-fields from them. Recognising this opportunity, in this paper we present an accessible tool for this purpose.

The basis of our kriging interpolation is explained in Section 2, and we outline its implementation in MATLAB in Section 3. Besides the flow-direction field, our method estimates planimetric convergence and curvature, which quantify the differential geometry of the reconstructed flowlines and are linked to the strain rates of the palaeo ice flow (Ng et al., in press). In Section 4 we apply the method to a flowset of the last British Ice Sheet. The numerical data and results of this case study as well as the MATLAB code are archived at doi:10.15131/shef.data.6735131. Although our exposition primarily refers to flowsets derived from populations of drumlins, crag-and-tails and MSGLs spanning tens to hundreds of kilometres, the method can be used on any type of palaeo ice-flow direction data and domains of vastly different sizes (e.g. glacial valleys where flow-direction data derive from striations, roche moutonées and flutes).

2. Method

2.1 General concepts and set-up

Over the timescales and lengthscales of interest, glaciers and ice sheets flow viscously with a velocity field describable by continuum mechanics. Given the low aspect ratios of most ice sheets and glaciers, we ignore the vertical component of velocity and regard the field as two-dimensional. This approximation breaks down for small ice masses on rugged terrain, but can be used if only the basal flow field is being reconstructed (as in our case since, strictly, subglacial bedforms record the flow direction of ice near its

base) and if the bed is near-planar, with a relief much less than the horizontal scale being considered.

We represent ice-flow direction at each position with the angle θ measuring clockwise from north ($-\pi < \theta \leq \pi$) or with an equivalent direction vector, and reconstruct the field $\theta(x, y)$ where x and y are horizontal coordinates (Figure 2a). The directions measured from subglacial bedforms comprising each flowset are samples of this field. Throughout the paper, we call these measurements our input data (/dataset), reserving the term flowset for the group of mapped bedforms from which they derive. Reconstruction requires finding from the input data an interpolation estimate of θ at any position. We expect θ to vary continuously and be differentiable almost everywhere. Notably, although the vectors of two neighbouring, differing measurements $\theta_1 \neq \theta_2$ meet when extended, the ice flow cannot "clash", due to mass conservation; i.e., flowlines in the area will converge or diverge but not intersect. Exceptions occur at singular points near ice-flow divides, summits and saddles, but these are sparse in the flow fields being reconstructed here as they typically lie in the areas between flowsets, and are thus already factored out.

Our approach follows established principles of kriging interpolation and is not fundamentally new, but contains non-standard features to overcome the problem of the 'circularity break' in θ at $-\pi : \pi$ (this discontinuity causes the θ-values of two similar directions on either side of south to differ substantially). Kriging is a geostatistical interpolation method that exploits the spatial structure of the measured/observed samples. It yields a best linear unbiased interpolation estimate by assuming that the field is an intrinsic random variable with spatial autocorrelative properties characterised by the variogram of the samples, which measures the variance of paired samples as a function of their separation distance. Kriging calculates the estimate as a linearly

weighted sum of the samples (kriging sum), whose coefficients (kriging weights) are optimised to minimise the expected mean square error between the estimate and the true value. For a further introduction, see the books by Isaaks and Srivastava (1989) and Kitanidis (1997). Kriging is suited to our problem because it can easily handle input data with irregular spacing, which are typical of glacial geological records. Its key steps are detailed in the next subsections and summarised in Figure 3. Gumiaux et al. (2003) outlined a methodology for kriging angular variables that focusses on geotectonic applications (e.g. strain patterns in rocks) and more on kriging orientation than direction. Our aim is similar, but we treat flow direction exclusively and supply essential equations and ready-to-use numerical code. Also we address an audience of glacial geomorphologists: The Geographic Information Systems software "ArcGIS" widely used in their studies can perform kriging but not on angular data, nor can it compile vectorial semi-variance (Section 2.2) for this purpose. These tasks are simple to code in languages such as MATLAB, R, Fortran and C, whose design for matrix computation makes them efficient for solving the large systems of simultaneous equations in kriging.

Our method entertains two aspects relevant to ice-flow reconstruction that have not been tackled together in the literature on direction/orientation kriging. First, when operating on the mapped directions of a flowset to estimate the flow field, the interpolation should undertake some "spatial smoothing"—in the sense that the kriged flow directions need not reproduce exactly the mapped directions (at their locations), but can deviate from them to portray a smoother field. Such smoothing is inherent in the qualitative approach, and is necessary because of uncertainty in the flow direction determined from each bedform. Some streamlined bedforms are irregularly shaped and lack a clear symmetry or axis portraying a direction. Moreover, that each bedform

records a unique direction is an idealisation, as the ice flow over it must have been three-dimensional at the bedform scale. Hence a sampled direction only approximates the local mean palaeo ice-flow direction. The level of smoothing required to suppress "measurement noise" due to these sources of uncertainty can be gauged from how much spatially-uncorrelated variability the input data contain, as quantified by the nugget of the variogram (Section 2.2). Below, we employ a version of kriging called Continuous Part Kriging (CPK), which uses the nugget to accomplish smoothing (Section 2.3).

A second aspect concerns the possibility of estimating ice flow convergence, C, and curvature, χ, during the interpolation. These geometrical measures quantify how fast flowlines merge or split and how fast they curve, respectively—regardless of flow speeds (Ng, 2015; Ng et al., in press). At each position, they are defined by the spatial derivatives (Ng, 2015; Ng et al., in press)

$$\mathrm{C}(\mathrm{x},\mathrm{y}) = \frac{\partial\theta}{\partial \mathrm{n}} \tag{1}$$

and

$$\chi(\mathrm{x},\mathrm{y}) = \frac{\partial\theta}{\partial \mathrm{s}}\ , \tag{2}$$

where n is distance in the direction left-perpendicular to flow and s is distance along flow (Figure 2a). Thus positive C and negative C describe converging and diverging ice flow, respectively; and positive (/negative) χ describes a rightward- (/leftward-) curving flow. A theory of the mathematical properties of C and χ has been given by Ng et al. (in press). Our method combines CPK with the computation of spatial derivatives to estimate the fields of C and χ from input data. Ice-flow convergence and divergence in plan view have been referred to in past glaciological analyses (e.g. Hambrey et al., 1999; Stokes and Clark, 2003), but the use of definitions (1) and (2) to quantify them is

a recent idea[1]. Ng (2015) computed a map of C for the Antarctic Ice Sheet from surface velocities measured from satellite data, and analysed C together with surface flow speeds to explore the complexity of ice-stream networks. His kriging method, outlined briefly in the Supplementary Materials of his paper, is what we detail herein.

We assume that each flowset and its lineations supplying input data to our method have been identified and mapped with sound glacial-geomorphological judgement. For instance, during mapping, each flow direction has been correctly interpreted from the two possibilities offered by a bedform orientation, and cross-cutting flowsets indicating multiple ice-flow events (e.g. shown by clustered orientations of different subsets of bedforms in the same area) have been separated correctly. In addition, only flowsets classified as "isochronous" (interpreted as recording ice flow at the same time) can be used; those classified as "time-transgressive" (built-up over a period of time, and thus incorporating temporal changes in ice-flow direction) are excluded (Clark, 1997). Finally, the bedform record may have been distorted or diminished by post-glacial erosion and sedimentation that alter the surface topography (Finlayson, 2013). Addressing these issues is beyond the scope of the present work.

2.2 Experimental and model variograms

Following standard practice, first we compile the experimental (or sample or empirical) variogram of the input direction data to quantify their spatial properties. A model fitted to this variogram is used to guide the kriging interpolation.

[1] Note that planimetric convergence and divergence here is not the same as the mathematical divergence of vector ice flux ($\nabla.\mathbf{q}$) in three dimensions; see Ng et al. (in press).

The variogram is a histogram plot of semi-variance γ—the statistical mean-squared difference between two observations—against their separation distance h. For a set of measurements $\mathbf{z}_i$, i = 1, 2, … m at the positions $\mathbf{x}_i = (x_i, y_i)$ (Figure 2a), semi-variance in each histogram bin of h is given by

$$\gamma(h) = \frac{1}{2M_h}\sum\left|\mathbf{z}_i - \mathbf{z}_j\right|^2 . \quad (3)$$

The sum is evaluated over all independent pairs of $\mathbf{z}_i$ and $\mathbf{z}_j$ ($i \neq j$) whose separation distance falls within the bin, and M_h is the number of those pairs (Isaaks and Srivastava, 1989; Kitanidis, 1997). The factor 1/2 corrects for reciprocal double-counting.

Taking flow direction θ directly as $\mathbf{z}$ in Equation (3) would lead to erroneous statistics due to the circularity break mentioned above; for instance, the difference between two θ-values near and on either side of south misrepresents the acute angle between them. To circumvent this problem we use Young's (1987) approach and measure vectorial semi-variance by defining $\mathbf{z}$ to be the direction vector

$$\mathbf{z}_i = (\sin\theta_i)\mathbf{e}_x + (\cos\theta_i)\mathbf{e}_y \quad (4)$$

($\mathbf{e}_x$ and $\mathbf{e}_y$ are unit vectors along the Cartesian axes) and quantifying the mismatch between flow directions by using the norm of the difference between direction vectors. Accordingly, the modulus $\left|\ \right|$ in (3) is executed as the vector norm (an equivalent approach is to express each direction as a complex number).

The experimental variograms of geospatial variables typically show γ in a rising trend with h, implying progressively less statistical correlation between two values as their separation increases. Thus nearby (/distant) observations should receive higher (/lower) weighting in the kriging interpolation. In a variogram displaying a well-defined sill (Figure 2b), the shoulder of the rise can be used to specify the kriging range R—the

radius beyond which observed samples are excluded from the interpolation because they are too weakly correlated with the desired estimate to be useful (Figures 2a and 2b). A larger R includes more samples and prolongs the kriging computation. In variograms with a rise but not a clear sill, R can be chosen as large as possible permitted by computing time constraints.

The nugget is the intercept value $C_0 = \gamma(h \to 0)$ indicated by the experimental variogram data (Figure 2b). A non-zero nugget reflects measurement error and the amount of uncorrelated noise or short (sub-grid) scale variability at vanishing separation. By definition $\gamma(h = 0) \equiv 0$ (see Equation (3)), so a variogram with non-zero nugget is discontinuous at the origin.

Next, a mathematical function approximating the experimental variogram—called the model variogram—needs to be decided. It is fed to the kriging stage for repeated evaluation. The model must be a certain "admissible function" or the sum of admissible functions to ensure positive definite covariances in the kriging such that the kriging variance (Equations (16) and (19) below) are positive (Armstrong, 1998). We refer the reader to Isaaks and Srivastava (1989) and Kitanidis (1997) for a range of commonly-used admissible functions, e.g. linear, Gaussian, exponential, spherical. For the variogram of the flowset in our case study (Figures 2c and 2d) we adopt a model that is the sum of a linear component and a Gaussian component:

$$\gamma(h) = C_0 + C_1 H + C_3\left[1 - e^{-(h/C_4)^2}\right], \tag{5}$$

where

$$H = \sqrt{h^2 + C_2^{\,2}} - C_2 . \tag{6}$$

The constants C_0 to C_4 are non-negative, and C_0 is the nugget discussed above. This choice of model is motivated by the finding that, for the particular flowset being studied, a Gaussian term capturing the shoulder of the experimental variogram at h ~ 40 km (Figure 2c) has an overly-flat profile for the first 10 km that severely mismatches the rising experimental data there (Figure 2d). The linear component is added for this reason. Separately, the substitution in Equation (6) modifies this component so that γ(h) bends to reach zero slope at h = 0 (Figure 2d)—the smaller is C_2, the shorter the distance over which this occurs. This local behaviour ensures spatial continuity and differentiabilty for the kriged variable (Kitanidis, 1997), as is required for the ice flow-direction field (Section 2.1). In many kriging applications, a visual fit of the model variogram to the experimental variogram suffices, or is done initially, followed by more precise tuning of selected model variogram parameters to optimise the performance of the kriged field (this does not mean a best fit to the experimental variogram itself, because this variogram serves mainly as a guide and its data distribution varies with the histogram bin choice). Figure 2c gives the final parameters C_0 to C_4 used in our case study. We detail their determination in Section 4.

2.3 Kriging interpolation

The interpolation estimate—or kriged estimate—at any position is the linearly weighted sum of nearby observations, specifically those lying within the chosen kriging range R. As described in the following, the kriging weights are found under constraints imposed by the model variogram. Since the model variogram encapsulates the spatial correlative properties of the field variable to be kriged, it serves a similar role as "operator experience" in the (existing) qualitative approach of conceptualising palaeo flow fields.

Let $\mathbf{z}_{0k}$ be the estimate sought at the position $\mathbf{x}_0 = (x_0, y_0)$. Suppose the observations within the search radius R are $\mathbf{z}_i$, i = 1, 2, … n and they lie at positions $\mathbf{x}_i$ (Figure 2a). These may include the position of interest $\mathbf{x}_0$. The kriging sum takes the form

$$\mathbf{z}_{0k} = \sum_{i=1}^{n} \lambda_i \mathbf{z}_i \tag{7}$$

where λ_i are the kriging weights. For an unbiased interpolation, the weights must satisfy the condition

$$\sum_{i=1}^{n} \lambda_i = 1 \, . \tag{8}$$

The weights are specific to each position $\mathbf{x}_0$. They vary from position to position as the configuration and number of observations in the search area change.

While the weights are scalar, $\mathbf{z}_i$ are the unit vectors of flow direction defined in Equation (4), so Equation (7) is a Fisher vectorial sum (Fisher, 1993; Gumiaux et al., 2003): the kriged estimate $\mathbf{z}_{0k}$ is a vector, typically of non-unit length. Conversion of $\mathbf{z}_{0k}$ to kriged flow direction θ_k is done by taking the arctangent of the ratio of its y-component to its x-component (our code uses the MATLAB function atan2 to put θ_k in the right quadrant, with $-\pi < \theta_k \leq \pi$). By carrying out the interpolation at different positions across the flowset domain, one can reconstruct the field $\theta_k(x, y)$.

We proceed to use Continuous Part Kriging (CPK) (Kitanidis, 1997; Chapter 7) to determine the weights λ_i. In this scheme, the variogram model is written as:

$$\gamma(h) = \begin{cases} \gamma_c(h) + C_0 & \text{for } h > 0 \\ 0 & \text{for } h = 0 \end{cases}, \tag{9}$$

where C_0 is the nugget and $\gamma_c(h)$ is the so-called "continuous part". This partitioning of γ recognises the observed data as the sum of random noise processes (which give rise to the nugget) and the underlying field variable to be reconstructed (the signal). By distinguishing $\gamma(h)$ and $\gamma_c(h)$ in the weight calculation, CPK filters out undesirable noise from the interpolation so that the reconstructed field $\theta_k(x, y)$ is smoothed. For the model in Equations (5) and (6), $\gamma_c = C_1[(h^2 + C_2^2)^{1/2} - C_2] + C_3[1 - \exp(-(h/C_4)^2)]$.

As in kriging elsewhere, the weights are found by solving a kriging system of simultaneous equations, which is derived by minimising the statistical expected mean-square interpolation error. The weights make Equation (7) a best estimator in this sense. We do not detail the derivation here (see Chapter 7 of Kitanidis (1997)) but simply state the kriging system:

$$-\sum_{j=1}^{n}\lambda_j\gamma_{ij} + v = -\gamma_{ci0} - C_0, \qquad i = 1, 2, \ldots n, \tag{10}$$

$$\sum_{j=1}^{n}\lambda_j = 1 \quad \text{(i.e. the unbiasedness condition).} \tag{11}$$

Here v is an unknown Lagrange multiplier, and γ_{ij} and γ_{ci0} are shorthands with the following meaning:

$$\gamma_{ij} = \gamma(|\mathbf{x}_i - \mathbf{x}_j|) \quad \text{and} \quad \gamma_{ci0} = \gamma_c(|\mathbf{x}_i - \mathbf{x}_0|)\,. \tag{12}$$

The modulus $|\ |$ refers to the vector norm as before.

There are n + 1 equations in (10) and (11) for calculating the n weights and v. The system is commonly expressed in matrix form as

$$\mathbf{M}\boldsymbol{\lambda} = \mathbf{b} \tag{13}$$

where

$$\mathbf{M} = \begin{bmatrix} -\gamma_{11} & -\gamma_{12} & \cdots & -\gamma_{1n} & 1 \\ -\gamma_{21} & -\gamma_{22} & \cdots & -\gamma_{2n} & 1 \\ \vdots & \vdots & & \vdots & \vdots \\ -\gamma_{n1} & -\gamma_{n2} & \cdots & -\gamma_{nn} & 1 \\ 1 & 1 & \cdots & 1 & 0 \end{bmatrix}, \tag{14}$$

$$\boldsymbol{\lambda} = \begin{bmatrix} \lambda_1 \\ \lambda_2 \\ \vdots \\ \lambda_n \\ \upsilon \end{bmatrix} \quad \text{and} \quad \mathbf{b} = \begin{bmatrix} -\gamma_{c10} - C_0 \\ -\gamma_{c20} - C_0 \\ \vdots \\ -\gamma_{cn0} - C_0 \\ 1 \end{bmatrix}. \tag{15}$$

Equation (13) is solved numerically for the vector $\boldsymbol{\lambda}$, whose first n elements are the kriging weights being sought.

In each evaluation of the kriging sum for $\mathbf{z}_{0k}$, the kriging variance is given by

$$\begin{aligned} \mathrm{E}[|\mathbf{z}_{0k} - \mathbf{z}_0|^2] &= -\upsilon + \sum_{i=1}^{n} \lambda_i \gamma_c(|\mathbf{x}_i - \mathbf{x}_0|) \\ &= -\upsilon + \begin{matrix} \lambda_1 & \lambda_2 & \cdots & \lambda_n \end{matrix} \begin{pmatrix} \gamma_{c10} \\ \gamma_{c20} \\ \vdots \\ \gamma_{cn0} \end{pmatrix} \end{aligned} \tag{16}$$

(E signifies expected value). This variance is a statistical estimate of the interpolation error based solely on the variogram and the spatial configuration of observed data in the search area. It will be large (i.e. the estimate $\mathbf{z}_{0k}$ is uncertain) if these data are few and lie near the edge of the kriging range. Since the kriging variance does not compare $\mathbf{z}_{0k}$ against any observed value of $\mathbf{z}_0$ (it doesn't even involve the observations $\mathbf{z}_i$), it does not measure the actual prediction/interpolation error.

Nonetheless, the kriging variance is useful as it can be computed across the domain as a field, and setting a maximum acceptable bound on it allows us to outline the area of reliably-reconstructed flow field. For this purpose, we translate it into a

standard deviation error having the unit of angle, by normalising its square root by $|\mathbf{z}_{0k}|$ and taking the inverse tangent; i.e.

$$\sigma_{\theta_k} = \arctan\left(\frac{\sqrt{\mathrm{E}[|\mathbf{z}_{0k} - \mathbf{z}_0|^2]}}{|\mathbf{z}_{0k}|}\right). \quad (17)$$

This approximate conversion recognises that fundamentally the kriging sum estimates a vector representing θ (not θ itself), and Equation (16) quantifies the error between vectors, rather than error in the kriged angular direction θ_k. In Section 2.5, we describe a way of gauging the true error on kriged estimates by using existing observations; that method, however, yields results only at the observed positions, not as a field.

2.4 Kriging convergence and curvature

Reconstructing palaeo ice-flow convergence C and curvature χ (Equations (1) and (2)) from the input data requires estimating directional derivatives. This is possible with the gradient-kriging approach developed by Philip and Kitanidis (1989). Here we combine this approach with CPK to estimate C and χ associated with the kriged direction field $\theta_k(x, y)$.

The basic idea is to apply the method of the last section to the position of interest $\mathbf{x}_0 = (x_0, y_0)$, and to a neighbouring position $\mathbf{x}_0^* = (x_0 + \Delta\sin\phi, y_0 + \Delta\cos\phi)$, where Δ is an incremental distance, and ϕ specifies the direction in which the spatial derivative is taken. Let us call the corresponding sets of kriging weights λ_i and λ_i^*, and the kriged estimates θ_k and θ_k^*. Then the kriged derivative of θ_k at $\mathbf{x}_0$ is given by

$$\mathrm{D}_{0k} = \lim_{\Delta \to 0} \frac{\theta_k^* - \theta_k}{\Delta}. \quad (18)$$

In the case of curvature ($\chi = D_{0k}$), we align the increment with the kriged flow direction by setting $\phi = \theta_k$. In the case of convergence ($C = D_{0k}$), we align it in the left-perpendicular direction and set $\phi = \theta_k - \pi/2$, so $(\sin\phi, \cos\phi) = (-\cos\theta_k, \sin\theta_k)$.

Philip and Kitanidis (1989) embedded this differentiation in the kriging minimisation and derived a new kriging system to estimate the gradient directly (their Equation (5)). But their system is tailored to non-circular scalar variables and cannot be applied to θ or $\mathbf{z}$. Therefore we follow the procedure in Equation (18) above. Two comments are in order for its numerical implementation. First, the matrix $\mathbf{M}$ depends on the distances between the observations $\mathbf{z}_i$ in the search radius (and on the variogram model). At each position of interest, these distances are the same when kriging for θ_k, kriging for θ_k^* in the curvature calculation, or kriging for θ_k^* in the convergence calculation; the only part of Equation (13) that changes is the vector $\mathbf{b}$ as we swap $\mathbf{x}_0$ for $\mathbf{x}_0^*$. Consequently, it is efficient to compute the inverse matrix $\mathbf{M}^{-1}$ once and use it three times for evaluating $\boldsymbol{\lambda} = \mathbf{M}^{-1}\mathbf{b}$. Second, care is needed when subtracting θ_k and θ_k^* in Equation (18) as these angles may straddle the break at $\pm\pi$. Given the small change Δ, we expect these angles to be similar and the angle $\Delta\theta = \theta_k - \theta_k^*$ to be acute or obtuse, not reflex. To ensure this, we subtract 2π from $\Delta\theta$ if $\Delta\theta > +\pi$ and add 2π to $\Delta\theta$ if $\Delta\theta \leq -\pi$ (this is done in the program `wraptopi.m`) before the division in Equation (18) We choose $\Delta = 1$ m in our calculations to approximate the limit.

Finally, the formula for kriging variance on the derivative of $\mathbf{z}_{0k}$ (obtained via Equation (4) of Philip and Kitanidis (1989)) is

$$\mathrm{E}[|D_{0k} - D_0|^2] = \left.\frac{d^2\gamma_c}{dh^2}\right|_{h\to 0} + \lim_{\Delta\to 0}\sum_{i=1}^{n}(\lambda_i^* - \lambda_i)\frac{\gamma_c(|\mathbf{x}_0 - \mathbf{x}_i + (\Delta\sin\phi, \Delta\cos\phi)|) - \gamma_c(|\mathbf{x}_0 - \mathbf{x}_i|)}{\Delta^2}. \quad (19)$$

The first term on the right-hand side here—the second derivative of γ_c—equals $C_1/C_2 + 2C_3/C_4^2$ for the variogram model in Equations (5) and (6). Conversion of Equation (19) to the kriging standard deviation (STD) in convergence and curvature (with the unit km^{-1}) is again done by normalising its square root by $|\mathbf{z}_{0k}|$.

2.5 Validation and calibration

How reliable is the reconstructed field $\theta_k(x, y)$? In other words, how well does the kriging predict ice-flow directions? We assess this by performing cross-validation, in which one observation is removed from the flowset at a time, and the other observations used to predict its value by kriging (Figure 3). At each observed position $\mathbf{x}_i$, the observation θ_i and its validation estimate θ_{vi} are then compared; this is an independent test because θ_i is not used in estimating θ_{vi}. A flowset of size n generates the same number of residuals $r_i = \theta_{vi} - \theta_i$, which should have near-zero mean and may be summarised into a root-mean-square (RMS) error quantifying the reconstruction's overall success. Since the observations contain uncertainty, even the best reconstruction will not reduce the RMS error to zero. This validation process will be illustrated in our case study. Note that cross-validation of the kriged fields of convergence and curvature is not possible due to the fundamental lack of independent observations of these variables, but the RMS is still a valid indicator of kriging success because C(x, y) and $\chi(x, y)$ are by-products of $\theta_k(x, y)$.

A related matter is calibration. The kriging outcomes—the reconstructed direction field and its RMS performance, and the reconstructed convergence and curvature fields and their kriging STDs—depend on the model variogram parameters. Consequently, after initial parameter estimates found from visual/manual fitting of the model to the experimental variogram (Section 2.2) are used in a first round of kriging, they can be

tuned to arrive at the "best" reconstruction. The optimisation used to achieve this in our case study is detailed in Section 4.

3. MATLAB Toolset

Figure 3 summarises the workflow of reconstructing the ice-flow field from a mapped flowset. In the order of execution, the key steps are: (i) preparation of input data (elaborated below), (ii) compiling the experimental variogram and selecting and fitting a model variogram, (iii) kriging interpolation with the input data constrained by the model variogram, (iv) validation of kriged flow directions, (v) calibration of kriging parameters to optimise the reconstruction and (vi) presentation of the output fields θ_k, C and χ. As in most other kriging practices, the method is interactive: user decision is needed in steps (ii) and (v).

We coded the method in a folder of MATLAB programs. This toolset, as well as the input data for "Flowset fs10" in our case study and its reconstructed fields, are given at doi:10.15131/shef.data.6735131. Readers wishing to familiarise with the programs can study the script file `process_fs10.m`, which lists the commands used to undertake a complete test run for Flowset fs10. By modifying these commands, the toolset can be applied to other flowsets. All results and plots produced in a run are stored in the sub-folder `/results`, which first needs to be created in the "home" folder containing the MATLAB programs. We briefly outline individual programs (e.g. `function.m`) in the following. More explanation of their input and output arguments can be displayed in MATLAB by using the workspace command "`help function`". Note that `.m` files named with the word "`example`" pertain to fs10, while the other files are generic.

Input data preparation

For a flowset containing n lineaments, the user prepares input data as a n-by-5 matrix F with the columns [Lineament_ID x_{start} y_{start} x_{end} y_{end}] and saves it to a MATLAB data file named `flowset.mat` in the home folder (see the `flowset.mat` in our toolset, for example). Each row of F refers to a lineament; Lineament_ID is its identification number specified by the user (it is not used in the kriging); x_{start} and y_{start} denote the lineament's start position, and x_{end} and y_{end} its end position. All distances/coordinates in our case study are measured in kilometres; if a different unit [L] is used (e.g. metre) then all distance/coordinate parameters should be in that unit, and the computed convergence and curvature have the unit $[L]^{-1}$. No special row ordering in F need to be observed. For bedforms whose outlines have been mapped, these need to be first converted to lineaments for F to be prepared, or converted to direction data (that is, θ, in radian) to form the matrix F_1 described below.

`lin_visual.m`: Plot the lineaments in matrix F in map view, in a colour specified by the user. A point is plotted to mark the start position (x_{start}, y_{start}) of each lineament.

`make_flowdir_matrix.m`: Load matrix F and create a n-by-3 matrix F_1 with the columns [x, y, θ], where x and y locate each lineament's midpoint, and θ is its direction in radian. Store F_1 in `flowset.mat`.

Variogram analysis

`find_vg.m`: Compile experimental variogram data (γ–h data pairs) from the position-direction data in F_1, using histogram bins whose edges increase from 0 to h_{max} in steps of dh. Both dh and h_{max} must be specified in the same unit as position. The user should choose h_{max} to be large enough so that any potential "sill" (Figure 2b) of the variogram

is not missed, and choose dh to be small enough to resolve the profile of the variogram, but not so small to limit the number of samples in each bin (typically, the resulting variogram will look excessively noisy in this case).

`compile_variogram_example.m`: Script file listing commands used to calculate experimental variogram data for Flowset fs10. This example uses `find_vg.m` twice, at a coarse resolution (dh = 5 km, h_{max} = 100 km) to capture the sill, and at a fine resolution (dh = 0.5 km, h_{max} = 10 km) to detail the variogram profile near the origin.

`variogram_model_manualfit_example.m`: Commands used to fit the model variogram in Equations (5) and (6) manually to the experimental variogram of fs10 and produce Figures 2c and 2d. The program plots the model curve and the experimental variogram data. The user specifies the parameters C_0 to C_4 on Line 20, and, by fitting the model to data through trial-and-error, determines the best parameter values.

Kriging interpolation

`krig_pos.m`: Calculate kriged estimates of flow direction θ_k, convergence C and curvature χ (and associated kriging STDs) at the position $\mathbf{x}_0 = (x_0, y_0)$ by Continuous Part Kriging, using the input data in F_1, kriging range R, and the variogram model in `vg_mod.m`. (This program calls the next three functions.) If the experimental variogram exhibits a sill, R should be chosen near where the sill begins, beyond the shoulder of the rise (Figure 2b). In the absence of a clear sill, R can be chosen as large as possible permitted by computing time constraints.

`krig_sys.m`: Assemble matrix **M** and vector **b** of the kriging system at the position of interest.

`vg_mod.m`: Evaluate the model variogram function in Equations (5) and (6). Different options yield γ, γ_c + C_0 and the derivative $d^2\gamma_c$ /dh^2 for use in the kriging equations (Sections 2.3 and 2.4).

`wraptopi.m`: Wrap the difference of two angles to the range $-\pi$ to $+\pi$ when subtracting them.

`krig_domain.m`: Use `krig_pos.m` to estimate the gridded fields of θ_k, C and χ across a rectangular domain and at the grid resolutions dx and dy specified by the user, and save the outputs to `results/kriging_results.mat`. The domain is defined by its edge positions in the vector [`xmin xmax ymin ymax`]. A typical choice is set it to contain an entire flowset. The output fields have the grid dimensions (`xmax`–`xmin`)/dx by (`ymax`–`ymin`)/dy (or to the nearest integers after rounding). Small values of dx and dy lead to a finely-resolved reconstruction, but demand long computation time.

`krig_fs10_example.m`: Commands used to reconstruct the gridded fields for Flowset fs10 in x = 330–430 km and y = 600–680 km at 0.5 km resolution (see Figures 5 and 6 and Section 4).

`trace_flowlines.m`: Starting from positions defined by mouse clicks in the domain, trace a flowline through each position by kriging the flow direction at successive locations both upstream and downstream; i.e. compute integral curves through θ_k(x, y).

Validation

`krig_validation.m`: Cross-validate the flow-direction kriging by computing the validation estimate θ_{vi} for each observation θ_i and compiling the list of residuals and their RMS (Section 2.5).

4. Case Study

4.1 Source data

Flowset fs10 is located in the Tweed Valley in the border region of Scotland and northeast England in the UK (Figure 4). It was used by Hughes et al. (2014) in their reconstruction of the evolution of flow dynamics of the British Ice Sheet (BIS) during the last glacial. These authors interpreted fs10 as an isochronous flowset, and, like earlier authors (e.g. Everest et al., 2005), as the imprint of a palaeo ice stream draining east towards the North Sea: the Tweed Ice Stream. The spatial pattern of subglacial bedforms that comprise fs10 (Figure 4) portrays convergent ice flow constrained by higher basal topography in the northwest, and to the south where the pattern curves around the Cheviot Hills. The precise age of this ice-flow event is uncertain. Hughes et al. (2014) assigned fs10 to Stage 7 in their relative chronology based on cross-cutting relationships between flowsets and glaciological consistency of flowset combinations at the ice-sheet scale; Stage 7 follows decoupling of the BIS from the Scandinavian Ice Sheet. By considering this assignment together with the absolute chronological envelope available at the time (Hughes et al., 2011) and marine-core evidence of ice-sheet activity in the North Sea, they placed Stage 7 in the early part of the period ~22–15 ka. Based on a compilation of absolute dates (Hughes et al., 2011) and a reconstruction of the retreat pattern of the BIS (Clark et al., 2012), the Tweed region was likely deglaciated between 17 and 16 ka, and this can be taken as a minimum age for the operation of the Tweed Ice Stream.

The mapped bedforms in fs10 consist of 1044 drumlins, 713 crag-and-tails and 248 MSGLs (Figure 4). Mapping was done from high-resolution surface DEM (NEXTMap Britain DEM from Intermap Technologies; 5 m cell size) and Landsat imagery (15 m cell size in panchromatic band) (Hughes et al., 2010). Crag-and-tails

were mapped as lineaments, MSGLs as lineaments, or as 'polylines' (a term in Geographic Information Systems meaning linked sequences of straight segments) if they curve, and drumlins as polygons tracing the outline along their topographic break-of-slope. The mapped data have been integrated into the BRITICE version 2 dataset (Clark et al., 2017). When gathering flow-direction input data for kriging, we converted the outline of each drumlin to a lineament by constructing its longest transect, which approximates the crest line of the drumlin.

We emphasise that other populous flowsets could be chosen to illustrate our method, and fs10 is used here not because it leads to more successful results, although several reasons make it an interesting and suitable choice. The bedforms in its area do not show pronounced cross-cutting that demands extensive flowset separation or implies a high risk of misappropriation of individual landforms; some cross-cutting occurs in its far southeast corner with another flowset and separation has already been done there (Hughes et al., 2014). Reconstructing the palaeo ice-flow field of fs10 can also yield quantitative data that enrich our understanding of Tweed Ice Stream; however, note that this paper's aim is chiefly methodological and not solely to deliver glaciological insights. Finally, fs10 shows a systematic distribution of bedform types, with MSGLs dominating its central part and drumlins and crag-and-tails occupying more peripheral regions (Figure 4). This raises the opportunity of performing a reconstruction with drumlins and crag-and-tails only and seeing how well the reconstructed flow field agrees with the mapped MSGL trajectories, which provide an independent record of the palaeo flowlines.

The most informed reconstruction would still employ the flow-direction measurements of all three bedforms. Therefore we undertook two specific reconstruction runs, one using the full flowset of drumlins, crag-and-tails and MSGLs,

and the other using a partial flowset excluding the MSGLs. We refer to these as "full" and "partial" reconstructions (or runs) below. The partial run mimics the scenario of a sparser flowset with larger gaps. A comparison of its outcome to that of the full run demonstrates how increased (/reduced) coverage and density of measurements improve (/degrade) a reconstruction. In the full reconstruction, the segments of each MSGL polyline are treated as lineaments. There are 632 MSGL segments in total, so the full input dataset has 2389 lineaments. In the partial reconstruction, the MSGL segments offer measured directions for comparison with the kriged flow directions.

As reported below, we also explored the effect of sparse input data by conducting reconstruction runs where the number of bedforms used in the input was successively reduced from the total available.

4.2 Flow-field reconstruction

The method of Sections 2 and 3 was applied to the full and partial input datasets. The experimental variograms of these datasets (Figures 2c and 2d) show the approximate nuggets of C_0 = 0.010 and 0.013, respectively. The first bin in h (0–0.5 km, Figure 2d) are ignored in this estimation because they are severely undersampled in terms of paired input data ($\mathbf{z}_i$ and $\mathbf{z}_j$ in Equation (3)) compared to larger bins. The full input dataset exhibits lower semi-variance than the partial dataset at all h. This is due to the low curvature of MSGLs, which enhances the spatial correlation between flow directions in the full dataset. For all of our reconstructions, we fixed the kriging range R at 50 km, beyond the shoulder of the rise of the experimental variogram data.

Our choice of the model variogram function in Equations (5) and (6) was justified in Section 2.2. Manual fitting of it to the experimental variograms yielded the parameters C_1 = 0.0025, C_3 = 0.28 and C_4 = 28 for the full input dataset and C_1 =

0.0038, C_3 = 0.40 and C_4 = 40 for the partial input dataset. The nuggets C_0 are as stated above. While C_1, C_3 and C_4 are well constrained by the long-range profiles of the binned data points and C_0 is well constrained by their apparent zero-intercepts, we found that C_2 is not: a sizeable range (~0.25–2) in this parameter gives plausible-looking fits. This is because C_2 determines the local curve shape of the model near h = 0 (Section 2.2), and this is difficult to gauge from the first few data points in h ≤ 2 km.

This curve shape near h = 0 controls the smoothness of the kriged fields of θ_k, C and χ and the expected errors on them. A large C_2 would flatten the curve so the model assigns similar semi-variance up to large h. Then observations within a large radius from the kriging position receive similar kriging weights, and the kriging resembles a "large-window averaging" operation that gives a very smooth output field θ_k and, accordingly, large errors between θ_k and θ-observations. We expect the opposite outcomes if C_2 is small. In contrast, the shape of the variogram model at h ≈ tens of km affects the outputs weakly because observations near the range R receive negligible kriging weights. These anticipated effects are consistent with conventional wisdom in kriging and confirmed by kriging test runs where we varied different parameters (see also discussion around Figure 6 below). Thus C_2 is the most sensitive parameter in the fitting. Consequently, we kept C_0, C_1, C_3 and C_4 at the above values and calibrated C_2 to maximise the overall kriging performance. Our rationale behind this optimisation is elaborated below. The final values of C_2 used are 1.0 in the full reconstruction and 0.8 in the partial reconstruction.

Figure 5 presents the results of the full reconstruction—its kriged fields of flow direction θ_k, convergence C and curvature χ (panels c, e, g) and the associated kriging standard deviations (STDs) (panels d, f, h). Figure 5a shows the present-day surface topography of the area, and Figure 5b plots sample flowlines computed with

`trace_flowlines.m` on the map of lineaments. The kriging STDs quantify uncertainty in the kriged fields. As expected, they are lower in areas more densely covered by lineaments (because more observations fall in the kriging range) and increase with distance away from the flowset overall. We use the 12° contour of the STD in θ_k to delineate a boundary for the usable reconstruction. This threshold is not definitive but allows us to block out uncertain areas when examining the reconstructed fields (Figures 5c, e, g). The kriging STDs in C and χ are similar and show a high ridge in the south-east corner of the domain, due to the tightly-curving pattern of lineaments surrounding this area.

The smoothing effect of our CPK method is evidenced by the smoothness of the reconstructed fields and flowlines, and by the mismatch between θ_k and measured flow directions at the latter's positions (compare flowlines with lineaments in Figure 5b). Cross-validation of θ_k in the full reconstruction yielded the residuals shown in Figure 6a. These residuals are uncorrelated and have a near-zero mean (0.0065°) and an RMS of 5.57°. They are largest for drumlins, smaller for crag-and-tails and smallest for the MSGL segments, reflecting more irregularity in the shape of drumlins and/or higher uncertainty when inferring ice-flow direction from them than the other two streamlined bedforms. The small residuals for MSGLs segments (RMS = 2.72°) attest their reliability as flow-direction indicators.

Two considerations enter our choice of the model-variogram parameter C_2. One of them is validation performance in θ_k in terms of the RMS. Multiple kriging experiments show that the RMS increases with C_2 (Figure 6b, black solid line) and does not vanish if $C_2 = 0$ (as is consistent with CPK; Section 2). A second consideration relevant to ice-flow reconstructions is uncertainty in C and χ. As these fields cannot be cross-validated, we assess this uncertainty by using their kriging STDs. The black dashed line in Figure

6b plots the mean kriging STD in C in the usable reconstruction area (within the 12° contour mentioned above); results for χ are almost the same. Raising C_2 smooths the convergence and curvature fields more, so they are less affected by short-scale error/variability in the lineament directions; thus, the STD measuring their statistical uncertainty decreases with C_2. Optimisation of C_2 would mean achieving low RMS for θ_k and low STD for C and χ as far as possible. But since these measures of error/uncertainty are incompatible (they have different units), the optimisation cannot be unique. Recognising this, here we decide reasonable values for C_2 in the full reconstruction (black dots, Figure 6b) and in the partial reconstruction (grey dots & curves, Figure 6b) by keeping both error measures acceptably low. In principle, a "cost function" combining these measures would enable a precise optimisation, if the practitioner knows how to weigh them against each other.

Turning to the reconstructed flow field, the flowlines (Figure 5b) depict a "main flow" that converges towards the northeast in its upstream part and becomes more parallel or weakly diverging as it turns towards the east and then southeast downstream; incoming flow joins it from the north. The downstream part can be interpreted as the trunk of the Tweed Ice Stream. Strong convergence in the western and northern halves of the flowset domain (Figure 5e) and a bipolar curvature distribution (Figure 5g; $\chi > 0$ in the trunk, $\chi < 0$ in the incoming flow) confirm this pattern. C and χ reach values of ± 0.2 km^{-1} and show spatial variations on length-scales down to several kilometres. We make further glaciological interpretations from Figure 5 in the next section.

Results in the partial reconstruction (Figure 7) are qualitatively similar but show greater uncertainty (compare grey dots with black dots in Figure 6b) and less detailed variations in the trunk, because its input data exclude MSGLs. The kriging STDs in the trunk are higher by ~70% in θ_k and ~160% in C than in the full run. Departures of the

partial run from the full run can be seen from scatterplots comparing θ_k, C and χ between these runs (Figures 8a–c). θ_k in the partial run can predict θ measured from MSGL segments to within an RMS error of 4° (Figure 8d). Two experiments with still smaller input datasets—one compiled from the drumlins only, the other from the crag-and-tails only—show that the reconstruction degrades further as more lineaments are excluded from the input (the reconstructed fields are not analysed here). The respective statistics in the same comparisons as those in Figures 8a–d (following the order of the figure panels) are Pearson R = 0.993, 0.828, 0.887 and 0.955 (with RMSE = 4.61°) for drumlins only, and Pearson R = 0.994, 0.757, 0.824 and 0.931 (with RMSE = 6.19°) for crag-and-tails only. These results demonstrate that small departures in θ_k can cause significant departures in the reconstructed convergence and curvature.

We investigated the effect of the spatial density of the input data more generally, by conducting additional reconstructions that used successively smaller subsets of fs10. First we removed 205 bedforms—chosen randomly, regardless of bedform type—from the total number of 2005 in fs10, to generate the input dataset for a run with 1800 bedforms. When a MSGL was chosen, all segments of its polyline were excluded. This procedure was repeated by removing 200 bedforms at a time. Thus we conducted nine runs with inputs compiled from bedforms numbering from 200 to 1800, in steps of 200. In contrast to the partial run (which used all drumlins and crag-and-tails, and no MSGLs), these runs imitate scenarios where all three types of bedforms are mapped but some have been missed. Note that a Monte-Carlo experiment using many different random successions of such sets of nine runs is also possible. This was not undertaken, as we wish to see only the typical trend of the results.

Following again the scheme of Figure 8, for each run we examined the correlations between the kriged values of θ_k, C and χ and those in the full reconstruction

(Figure 9a) and how well θ_k predicts the colocated flow directions measured from MSGL segments in our full dataset (Figure 9b). As expected, the reconstruction progressively deviates from the full reconstruction as the size of the input dataset is reduced. While departures in kriged flow directions are minimal (Pearson R > 0.95 in Figures 9a and 9b; RMS error < 4° in Figure 9b), the kriged convergence and curvature fields degrade strongly when the input uses fewer than ~500 bedforms—when their mean spatial density falls below ~0.2 km^{-2}. Importantly, since we have studied only one flowset, this density and these findings do not necessarily reflect the minimum input-data requirement for achieving a reasonable or robust reconstruction with other flowsets, whose kriging outcomes may depend differently on the bedform abundance, distribution and orientation used in the input. Figures 9c and 9d show two of the flow fields reconstructed in the run using 200 bedforms. While the reconstructed flowline pattern visually resembles the ones in Figures 5b and 7b, the reconstructed convergence field is noticeably smoother and short of detailed features (cf. Figures 5e and 7c).

4.3 Palaeo-glaciological findings

What do we learn from the full reconstruction about the configuration and dynamics of Tweed Ice Stream? We analyse here the reconstructed fields alongside the bed topography (Figure 5a) and the bedform distribution in the flowset.

While the overall impression of flow converging into the purported ice-stream trunk can be gained from the flowset without tracing precise flowlines, the reconstruction quantifies the pattern with novel information. The convergence and curvature fields have magnitudes on the order of $\pm 10^{-1}$ km^{-1} (Figure 5), as seen on Antarctic ice-stream networks (see Figure 1 of Ng, 2015). In the upstream part of the trunk, the reconstructed flow is markedly non-uniform and shows strong convergence

interspersed with divergence (Figure 5e). The corresponding "ripples" of convergence, with spacing of a few to ~10 km and axes sub-parallel to the flow direction (Figure 5e), are commonly found on contemporary ice streams, especially in their onset zones and tributaries where ice flow accelerates (Ng, 2015). In the full reconstruction, ripples in curvature oriented transversely to the flow (Figure 5g) accompany the convergence ripples, highlighting irregularities of the flow field. Comparison of Figures 5e and 5g with the bed DEM in Figure 5a shows that the ripple amplitudes are strongest in the upper part of the Tweed Valley where the underlying topography is rugged (area enclosed by dashed curves in Figures 5a, e and g). Their amplitudes decay into the trunk where the bed relief is low. This correlation suggests that the ripples record perturbations of the ice flow by undulating bed topography (Gudmundsson, 2003; Ng et al., in press) on length-scales of several to ~10 km. We identify three sites (ellipses in Figures 5a and 5e) where a prominent basal ridge or bump seems to have caused flow divergence on its stoss side and convergence on its lee side. Similar "dipoles" in C have been observed on the Antarctic Ice Sheet (Ng, 2015; Ely et al., 2017).

Another discovery from the reconstruction which corroborates the idea that Flowset fs10 records ice-stream flow is evidence of the lateral shear margins of flow. In Figure 3 of their paper, Everest et al. (2005) delineated the locations of the northern and southern margins of Tweed Ice Stream, which we reproduce here in Figures 4 and 9. The identification of these margins by these authors appears to be based on the transition between streamlined and non-streamlined bed surfaces and/or where the smooth valley floor meets the higher relief of the uplands. Our reconstruction reveals the ice stream's lateral margins in a different way. The convergence field shows strongly positive C-values along two distinct stretches, as indicated by the two bold dashed lines in Figure 5e. The northern stretch is about 25 km long; flowlines funnel

tightly towards it from upstream and cross obliquely into its southern side (Figure 5b). This stretch coincides with a boundary between drumlins to the north and the considerably longer MSGLs to the south (Figures 4 and 10a). By assuming tentatively that drumlins reflect slower ice flow and MSGLs faster ice flow, we infer a distinct speed change that indicates shearing across the boundary. The C-values along the stretch are 0.1–0.2 km^{-1} (with low kriging STDs $\lesssim$0.04 km^{-1}), similar to those observed for Antarctic ice-stream shear margins (Ng, 2015). Together, the convergence signature, the shearing implied by the bedform-length transition, and the flowline pattern surrounding the stretch identify it as the northern ice-stream shear margin. Its position, which is unchanged if we located it with the partial reconstruction (Figure 7c), lies several kilometres south of the margin mapped by Everest et al. (2005) (Figures 4 and 10a). The northern limit of Flowset fs10 as inferred by Hughes at al. (2014) is also further north of this margin, indicating that this flowset includes both the ice stream and contributing flow from slower-moving tributaries. Our inspection of this margin using multiple hill-shaded renditions of the NEXTMap Britain DEM (e.g. Figure 10a) shows that despite the clear change in bedform imprint across it, no shear-margin moraine is visible.

Similarly, we identify the other convergent stretch in Figure 5e as the southern ice-stream margin. Its upstream part deviates from the southern margin located by Everest et al. (2005) (Figures 4 and 10b). This ice-stream margin seems to be largely controlled by the underlying bed topography, as it lies at the base of the northern slope of the Cheviot Hills (Figure 10b). As shown by Figure 4, the ice-stream trunk in our reconstruction is rather uniform in width (≈ 18 km) and does not narrow as sharply as in the reconstruction by Everest et al. (2005).

5. Discussions and Conclusion

We have presented a tool (with MATLAB implementation) for estimating palaeo ice-flow fields by kriging the flow directions recorded by subglacial bedforms. Any point data with a direction value can be used as input, including those derived from striations as well as streamlined bedforms such as drumlins and MSGLs. The method is a step forward from the traditional approach of relying on human vision to conceptualise the flow field, which does not yield quantitative results. Application of the method to a flowset from the Tweed Valley, NE England (Section 4) demonstrates its feasibility, the level of detail achievable in the reconstructed fields (Figure 5) and the potential of using these for glaciological interpretations. We conclude by commenting on general aspects of the method and anticipating applications for its use.

Does the method succeed? Let us emphasise first that kriging interpolation always "works": the key question is whether the input data portray a coherent pattern such that the kriged flow field is reliable. The level of coherence, as reflected by the kriging deviations on θ_k, C and χ (e.g. Figures 5d, f, h), depends on the density and distribution of lineaments and their spread of directions, and may vary across a flowset. Lower density and higher spread are expected to give a less certain flow field.

However, our method is not without caveats or room for development. In the toolset we assembled, the user needs to fit the model variogram and choose key kriging parameters (range, nugget) manually. Although this procedure can be done via computerised optimisations that minimise the misfit, the potential diversity of experimental-variogram data for different flowsets means that it cannot be fully automated (sometimes or some user intervention is necessary). It is important to note that kriging is not entirely free of subjectivity—some subjectivity lies in those choices. But unlike in the human-visual approach, the choices are informed by experimental-

variogram data (which replace the operator's experience and perception of patterns in a flowset), and both the sensitivity of the reconstructed flow fields to those choices and uncertainty estimates for the fields are reproducible.

In this connection, our kriging scheme assumes the same autocorrelative properties (the same model variogram) for observations lying in different directions around each position where an estimate is sought. Not having investigated the directionality of the experimental variograms of many flowsets, at this stage we do not know how widespread is anisotropy in the correlative properties of glacial flow fields and whether some flowsets demand more sophisticated treatment—see Friedland et al. (2017) for an application of anisotropic kriging to wind-speed data. Also, interpolation methods such as Inverse Distance Weighting has not been explored here. It may be useful to compare them (after adaptation for angular data) against kriging, as has been done in other geoenvironmental settings (e.g. Zimmerman et al., 1999; Lu and Wong, 2008).

In the palaeo ice-sheet reconstruction context, flow fields computed by our method cannot be independently validated if all relevant direction measurements have been used as input; only cross-validation is possible (Section 2.5). This limitation is also true for the traditional qualitative approach. Neither do flow fields simulated by thermomechanical models of palaeo ice flow offer an independent validation, as quite likely they are to be tested against our reconstruction, which is constrained by bedform observations. A way of testing our method extensively is to use observations from contemporary ice sheets, by sub-sampling their flow directions to feed into our method and using the rest to evaluate its performance.

Our method is readily applicable to the large number of flowsets and directional glacial bedforms reported in the literature and archived in projects such as BRITICE

(Clark et al., 2017), which include bedforms mapped from terrestrial surfaces, by acoustic sounding of submarine surfaces (e.g. Dowdeswell et al., 2016), and by radar sounding of present-day subglacial topography (e.g. King et al., 2016). In gathering the input flow-direction data, MSGLs can be segmented as done in the Tweed Valley study. As we learned from this case study, the reconstructed ice-flow fields may help us recognise sub-units of flow and characterise or locate dynamical features (e.g. shear margins, convergence dipoles) that are difficult to discern otherwise. Thus there is opportunity to enrich the large-scale ice-sheet reconstructions with detailed flow-structure analyses. In these reconstructions, flowsets can also be classified by their (areal-averaged) kriging uncertainty to inform decisions behind interpretations of the ice-sheet history and dynamics. Another possibility is systematic study of the patterns of convergence and curvature of palaeo ice streams, which can be done alongside the study of contemporary ice streams (Ng, 2015).

In the exacting process from bedform mapping to reconstructing an ice sheet's history, one of the most important steps is in the grouping of bedforms/lineaments into flowsets. Erroneous groupings can mislead or introduce errors into the final reconstruction. This step involves deciding whether lineaments in an area belong to one flowset or to multiple (cross-cutting or adjacent) flowsets—and in the latter case, deciding to which flowset they belong. This pattern recognition is non-trivial and has so far been performed manually (e.g. Greenwood and Clark, 2009) and therefore may vary due to skill and experience between practitioners. Our tool can be used to check its outcome, and potentially to test the plausibility of different flowset groupings. Notably, flowsets classified as isochronous but found to have statistically high kriging uncertainty on their reconstructed ice-flow fields, may lead one to query their isochroneity and decide whether further subdivision into multiple flowsets is required.

Across many flowsets, one may expect the population of time-transgressive flowsets to have statistically higher kriging uncertainty than the isochronous population.

Our reconstruction method may more specifically aid the separation of cross-cutting flowsets. These flowsets result from the superposition of imprints of different ice-flow events at different times leading to a palimpsest landscape of ice-flow signatures, a cumulative result of ice-flow history over an area. Suppose a preliminary choice has been made to disentangle two cross-cutting flowsets. The cross-validation residuals found from kriging their ice-flow fields (e.g. Figure 6a) may identify some lineaments whose directions fit poorly with the reconstructed flowlines; i.e. they have large residuals in θ. These lineaments can be selectively reassigned to the other flowset to find the combination that optimises the fit for all lineaments and the kriging STDs of both reconstructed fields. Recently, Smith et al. (2016) developed a semi-automated algorithm for separating cross-cutting flowsets that employs the statistics (notably, clusteredness) of bedform directions and lengths. Our idea here can be integrated with their algorithm to refine the separation. We leave this challenge to future work. Also on the horizon are prospects of using artificial intelligence to tackle the pattern-recognition tasks in ice-sheet reconstructions based on geological datasets. Our current study is partly motivated by the fact that such an approach requires quantitative analyses of data.

Finally, our method may be used to derive contextual information on palaeo ice-flow configurations for the study of subglacial geomorphological and sedimentological processes—for instance, investigations of how ice-flow direction relates to the development of preferred orientation in till fabrics (e.g. Iverson, 2017) or directional anisotropy in bed topographic roughness (e.g. Spagnolo et al., 2017). Furthermore, there has been a growing literature that amasses and analyses morphometric data of subglacial bedforms (Clark et al., 2009; Hess and Briner, 2009; Spagnolo et al., 2010, 2011;

Maclachlan and Eyles, 2013; Ely et al., 2016; Livingstone et al., 2016) to infer the processes and factors behind their genesis, sculpting and preservation. Knowledge of the palaeo ice-flow conditions (e.g. basal stress and velocities) during subglacial bedform formation has hitherto, been mostly or entirely lacking from such analyses because the ice is no longer present. With our method, convergence and curvature are novel parameters of the flow that can now be reconstructed and involved in these analyses.

Note: The files of our toolset and computed data are accessible via https://figshare.com/s/a860caa183b33d8baf42 while the archival site doi:10.15131/shef.data.6735131 awaits activation.

Acknowledgements

FN acknowledges the generous support of a Leverhulme Trust Research Fellowship in 2017-18 (no. RF-2017-320). Mapping of Flowset fs10 was conducted by ALCH at the University of Sheffield during her PhD, which was funded by the UK Natural Environment Research Council and British Geological Survey (Studentship NER/S/A/2004/12102). The elevations in Figure 5a derive from Ordnance Survey Terrain 50 and contain OS data © Crown copyright and database right 2017. We thank M. Winsborrow, S. Greenwood, M. Spagnolo, C. Clark and I. Barr for discussions about flowsets during “Image Workshops” in 2005-2008 in the Department of Geography, University of Sheffield. We thank S. Livingstone, G. Mallon and C. Clark for valuable comments on the manuscript, and R. Storrar and M. Spagnolo for providing helpful reviews and suggestions. The authors declare no conflict of interest.

References

Armstrong M. 1998. Basic Linear Geostatistics. Springer.

Clark CD. 1997. Reconstructing the evolutionary dynamics of former ice sheets using multi-temporal evidence, remote sensing and GIS. Quaternary Science Reviews **16**: 1067–1092.

Clark CD, Knight JK, Gray JT. 2000. Geomorphological reconstruction of the Labrador Sector of the Laurentide Ice Sheet. Quaternary Science Reviews **19**: 1343–1366.

Clark CD, Hughes ALC, Greenwood SL, Spagnolo M, Ng FSL. 2009. Size and shape characteristics of drumlins, derived from a large sample, and associated scaling laws. Quaternary Science Reviews **28**: 677–692.

Clark CD, Hughes ALC, Greenwood SL, Jordan C, Sejrup HP. 2012. Pattern and timing of retreat of the last British-Irish Ice Sheet. Quaternary Science Reviews **44**: 112–146.

Clark CD and 13 others. 2017. BRITICE Glacial Map, version 2: a map and GIS database of glacial landforms of the last British–Irish Ice Sheet. Boreas **47**: 11–27. doi:10.1111/bor.12273.

Dowdeswell, JA, Canals M, Jakobsson M, Todd BJ, Dowdeswell EK, Hogan KA. 2016. Atlas of Submarine Glacial Landforms: Modern, Quaternary and Ancient. Geological Society of London.

Ely JC, Clark CD, Spagnolo M, Stokes CR, Greenwood SL, Hughes ALC, Dunlop P, Hess D. 2016. Do subglacial bedforms comprise a size and shape continuum? Geomorphology **257**: 108–119. doi:10.1016/j.geomorph.2016.01.001.

Ely JC, Clark CD, Ng FSL, Spagnolo M. 2017. Insights on the formation of longitudinal surface structures on ice sheets from analysis of their spacing, spatial distribution,

and relationship to ice thickness and flow. Journal of Geophysical Research – Earth Surface **122**: 961 –972. doi:10.1002/2016JF004071.

Everest J, Bradwell T, Golledge N. 2005. Subglacial landforms of the Tweed Palaeo-Ice Stream. Scottish Geographical Journal **121**: 163–173. doi:10.1080/00369220518737229.

Finlayson A. 2013. Digital surface models are not always representative of former glacier beds: Palaeoglaciological and geomorphological implications. Geomorphology **194**: 25–33. doi:10.1016/j.geomorph.2013.03.026.

Fisher, NI. 1993. Statistical Analysis of Circular Data. Cambridge University Press: Cambridge.

Friedland CJ, Joyner TA, Massarra C, Rohli RV, Treviño AM, Ghosh S, Huyck C, Weatherhead M. 2017. Isotropic and anisotropic kriging approaches for interpolating surface-level wind speeds across large, geographically diverse regions. Geomatics, Natural Hazards and Risk **8**: 207–224. doi:10.1080/19475705.2016.1185749.

Greenwood SL, Clark CD. 2009. Reconstructing the last Irish Ice Sheet 1: changing flow geometries and ice flow dynamics deciphered from the glacial landform record. Quaternary Science Reviews **28**: 3085–3100.

Gudmundsson, GH. 2003. Transmission of basal variability to a glacier surface. Journal of Geophysical Research **108**: 2253. doi:10.1029/2002JB002107.

Gumiaux C, Gapais D, Brun JP. 2003. Geostatistics applied to best-fit interpolation of orientation data. Tectonophysics **376**: 241−259.

Hambrey MJ, Bennett MR, Dowdeswell JA, Glasser NF, Huddart D. 1999. Debris entrainment and transfer in polythermal valley glaciers. Journal of Glaciology **45**: 69-86.

Hess DP, Briner JP. 2009. Geospatial analysis of controls on subglacial bedform morphometry in the New York Drumlin Field — implications for Laurentide Ice Sheet dynamics. Earth Surface Processes and Landforms **34**: 1126–1135.

Hubbard A, Bradwell T, Golledge N, Hall A, Patton H, Sugden D, Cooper R, Stoker M. 2009. Dynamic cycles, ice streams and their impact on the extent, chronology and deglaciation of the British-Irish ice sheet. Quaternary Science Reviews **28**: 758–776.

Hughes ALC, Clark CD, Jordan CJ. 2010. Subglacial bedforms of the last British Ice Sheet. Journal of Maps **6**: 543–563. doi:10.4113/jom.2010.1111.

Hughes ALC, Clark CD, Jordan CJ. 2014. Flow-pattern evolution of the last British Ice Sheet. Quaternary Science Reviews **89**: 148–168.

Hughes ALC, Greenwood SL, Clark CD. 2011. Dating constraints on the last British-Irish Ice Sheet: a map and database. Journal of Maps **7**: 156–184. doi:10.4113/jom.2011.1145.

Isaaks EH, Srivastava RM. 1989. Applied Geostatistics. Oxford University Press: New York.

Iverson NR. 2017. Determining glacier flow direction from till fabrics. Geomorphology **299**: 124 –130.

King EC, Pritchard HD, Smith, AM. 2016. Subglacial landforms beneath Rutford Ice Stream, Antarctica: detailed bed topography from ice-penetrating radar. Earth System Science Data **8**: 151–158. doi:10.5194/essd-8-151-2016.

Kitanidis PK. 1997. Introduction to Geostatistics: Applications in Hydrogeology. Cambridge University Press: Cambridge.

Kleman J, Borgström I. 1996: Reconstruction of palaeo-ice sheets: The use of geomorphological data. Earth Surface Processes and Landforms **21**: 893–909.

Kleman J, Hättestrand C, Borgström I, Stroeven A. 1997. Fennoscandian palaeoglaciology reconstructed using a glacial geological inversion model. Journal of Glaciology **43**: 283–299.

Kleman J, Hättestrand C, Stroeven AP, Jansson KN, De Angelis H, Borgström I. 2006. Reconstruction of paleo-ice sheets - inversion of their glacial geomorphological record. In Glacier Science and Environmental Change, Knight PG (ed), Blackwell Science Ltd: Oxford; 192–198.

Li YK, Napieralski J, Harbor J, Hubbard A. 2007. Identifying patterns of correspondence between modeled flow directions and field evidence: An automated flow direction analysis. Computers and Geosciences **33**: 141–150.

Livingstone SJ, Stokes CR, Cofaigh CÓ, Hillenbrand C-D, Vieli A, Jamieson SSR, Spagnolo M, Dowdeswell JA. 2016. Subglacial processes on an Antarctic ice stream bed. 1: Sediment transport and bedform genesis inferred from marine geophysical data. Journal of Glaciology **62**: 270 –284.

Lu GY, Wong DW. 2008. An adaptive inverse-distance weighting spatial interpolation technique. Computers and Geosciences **34**: 1044–1055.

Maclachlan JC, Eyles CH. 2013. Quantitative geomorphological analysis of drumlins in the Peterborough drumlin field, Ontario, Canada. Geografiska Annaler: Series A, Physical Geography **95**: 125–144.

Marshall SJ, Tarasov L, Clarke GKC, Peltier WR. 2000. Glaciological reconstruction of the Laurentide Ice Sheet: physical processes and modelling challenges. Canadian Journal of Earth Sciences **37**: 769–793.

Ng FSL. 2015. Spatial complexity of ice flow across the Antarctic Ice Sheet. Nature Geoscience **8**: 847–850. doi:10.1038/ngeo2532.

Ng FSL, Gudmundsson GH, King EC. In press. Differential geometry of ice flow. Frontiers in Earth Science – Cryospheric Sciences. Details to be known soon. doi:10.3389/feart.2018.00161.

Ng FSL, Ignéczi A, Sole AJ, Livingstone SJ. 2018. In press. Response of surface topography to basal variability along glacial flowlines. Journal of Geophysical Research – Earth Surface. Details to be known soon. doi:10.1029/2017JF004555.

Patton H, Hubbard A, Andreassen K, Auriac A, Whitehouse PL, Stroeven AP, Shackleton C, Winsborrow M, Heyman J, Hall AM. 2017. Deglaciation of the Eurasian ice sheet complex. Quaternary Science Reviews **169**: 148–172.

Philip RD, Kitanidis PK. 1989. Geostatistical estimation of hydraulic head gradients. Ground Water **27**: 855−865.

Rose J, Letzer JM. 1977. Superimposed drumlins. Journal of Glaciology **18**: 471–480.

Saha K, Wells NA, Munro-Stasiuk M. 2011. An object-oriented approach to automated landform mapping: a case study of drumlins. Computers and Geosciences **37**: 1324–1336.

Spagnolo M, Clark CD, Hughes ALC, Dunlop P, Stokes CR. 2010. The planar shape of drumlins. Sedimentary Geology **232**: 119–129.

Spagnolo M, Clark CD, Hughes ALC, Dunlop P. 2011. The topography of drumlins; assessing their long profile shape. Earth Surface Processes and Landforms **36**: 790–804. doi:10.1002/esp.2107

Spagnolo M, Bartholomaus TC, Clark CD, Stokes CR, Atkinson N, Dowdeswell JA, Ely JC, Graham AGC, Hogan KA, King EC, Larter RD, Livingstone SJ, Pritchard HD. 2017. The periodic topography of ice stream beds: Insights from the Fourier spectra of mega-scale glacial lineations. Journal of Geophysical Research – Earth Surface **122**: 1355–1373. doi:10.1002/2016JF004154.

Smith MJ, Anders NS, Keesstra SD. 2016. CLustre: semi-automated lineament clustering for palaeo-glacial reconstruction. Earth Surface Processes and Landforms **41**: 364–377.

Stokes CR, Clark CD. 1999. Geomorphological criteria for identifying Pleistocene ice streams. Annals of Glaciology **28**: 67–75.

Stokes CR, Clark CD. 2003. The Dubawnt Lake palaeo-ice stream: evidence for dynamic ice sheet behaviour on the Canadian Shield and insights regarding the controls on ice-stream location and vigour. Boreas **32**: 263–279. doi:10.1080/03009480310001155.

Tarasov L, Peltier WR. 1999. Impact of thermomechanical ice sheet coupling on a model of the 100 kyr ice age cycle. Journal of Geophysical Research – Atmospheres **104**: 9517–9545.

Winsborrow MCM, Andreassen K, Corner GD, Laberg JS. 2010. Deglaciation of a marine-based ice sheet: Late Weichselian palaeo-ice dynamics and retreat in the southern Barents Sea reconstructed from onshore and offshore glacial geomorphology. Quaternary Science Reviews **29**: 424–442.

Young DS. 1987. Random vectors and spatial analysis by geostatistics for geotechnical applications. Mathematical Geology **19**: 467−479.

Zimmerman D, Pavlik C, Ruggles A, Armstrong MP. 1999. An experimental comparison of ordinary and universal kriging and inverse distance weighting. Mathematical Geology **31**: 375 –390.

Figure Captions

Figure 1. Steps of reconstructing paleo ice-flow event from streamlined bedforms. (a) Mapping of bedforms as lineaments on source satellite imagery or digital topography of the deglaciated land surface. The example shown derives from the NEXTMap Britain DEM. Its location is unimportant as the other panels are hypothetical. (b) Lineaments identified as belonging to an isochronous flowset. (c) Ice-flow event conceptualised from the lineament pattern. (d) Palaeo ice flowlines traced on a continuous field of ice-flow direction that has been estimated from direction vectors (arrows) derived from the mapped lineaments. The manual, qualitative step from (b) to (c) is the traditional method. This paper describes a quantitative method for the step from (b) to (d) that uses kriging to reconstruct the palaeo ice-flow direction field.

Figure 2. (a) Symbols used to describe the flow-direction field $\theta(x, y)$ and observed data, and definition of convergence C and curvature χ. Observations are shown as unit vectors. Kriging at a point of interest $\mathbf{x_0}$ uses observations within the range R. (b) Schematic of an experimental variogram and a model used to approximate it. (c, d) Experimental and model variograms for Flowset fs10 of our case study. Panel d enlarges the area in c near the origin. Experimental-variogram data are compiled at two bin sizes for the full flowset of drumlins, crag-and-tails and MSGL segments (black) and a partial flowset excluding MSGL segments (grey). Model curves plot Equations (5) and (6) evaluated using the parameters listed in panel c.

Figure 3. Overview of our kriging method of ice-flow field reconstruction. MATLAB programs performing key tasks are named in italics. User decision is required for

choosing the variogram model, fitting it to the experimental variogram and optimising its parameters. Validation and calibration pathways are dashed for clarity.

Figure 4. The Tweed Valley region and distribution of streamlined bedforms in Flowset fs10 identifed by Hughes et al. (2014). Bedforms mapped in the area but associated with other flowsets are not shown. Coordinates are in British National Grid. Background portrays surface elevations from the Ordnance Survey (OS) Terrain 50. The general palaeo ice-flow direction is from west to east. The lateral margins of Tweed Ice Stream inferred by Everest et al. (2005) and inferred from our reconstructed flow field and the areas enlarged in Figure 10 are indicated.

Figure 5. Results of palaeo ice-flow field reconstruction for Flowset fs10 using its full input dataset of drumlins, crag-and-tails and MSGLs. All reconstructed fields are given at 0.5 km resolution. (a) Bed topography from the OS Terrain 50 digital elevation model (50 m cell size). (b) Reconstructed flowlines overlain on the mapped lineaments. Kriged fields of (c) flow direction, (e) convergence and (g) curvature, and the corresponding fields of kriging standard deviations (d, f, h). Thick dashed lines mark ice-stream margins inferred from the convergence field in (e). Thin dashed curve highlights prominent convergence and curvature ripples. Ellipses in (a) and (e) locate basal bumps and the associated convergence dipoles. In the panels on the right, the short traces depict bedform lineaments; thin white loops mark the 12° contour in kriging standard deviation in flow direction.

Figure 6. (a) Residuals of kriged flow direction at the positions of lineaments, found from cross-validation of the full reconstruction with C_2 = 1.0. (b) Impact of model-

variogram parameter C_2 on the RMS of the cross-validation residuals (solid lines; left-hand axis) and on the mean kriging STD in convergence (dashed lines; right-hand axis) in the full reconstruction (black) and the partial reconstruction (grey). Vertical lines indicate our choices of C_2 in these reconstructions.

Figure 7. Key results of palaeo ice-flow reconstruction with Flowset fs10 using a partial input dataset of only drumlins and crag-and-tails. (a, c, d) Kriged fields of flow direction, convergence and curvature. (b) Traced flowlines and lineaments used in the reconstruction. Dashed lines are the ice-stream margins from Figure 5.

Figure 8. (a to c) Correlation between reconstructed flow direction, convergence and curvature in the partial reconstruction (vertical axes) and their values at the same grid locations in the full reconstruction (horizontal axes). (d) Observed flow direction derived from MSGL segments versus flow direction predicted by the partial reconstruction at their mid-point locations. All four correlations are statistically significant with $p << 0.05$.

Figure 9. Performance of nine additional reconstructions that use different subsets (reduced numbers) of the bedforms in Flowset fs10 as input. (a) Correlation between flow direction θ_k, convergence C and curvature χ reconstructed in each run and their values at the same grid locations in the full reconstruction. The line shows the mean spatial density of bedforms in each run, calculated from their abundance and the approximate bounding area of the flowset (≈ 2550 km^2). (b) Correlation between flow directions reconstructed in each run at the mid-points of MSGL segments and observed flow directions inferred from those segments. (c) Lineaments used in the run employing

200 bedforms (i.e., the first run in panels a and b) and the corresponding reconstructed flowlines. (d) Kriged convergence field in the run using 200 bedforms.

Figure 10. Locations of the (a) northern and (b) southern lateral shear margins of Tweed Ice Stream inferred from the ice-flow convergence field of our reconstruction, compared to those delineated by Everest et al. (2005) through interpreting the geomorphological signature alone. Background shows hill-shaded surface topography based on the NEXTMap Britain DEM. The two regions are outlined in Figure 4. In both panels, some streamlined bedforms lie outside the margin located by us, and we see no shear margin moraine on the DEM.

Figure 1

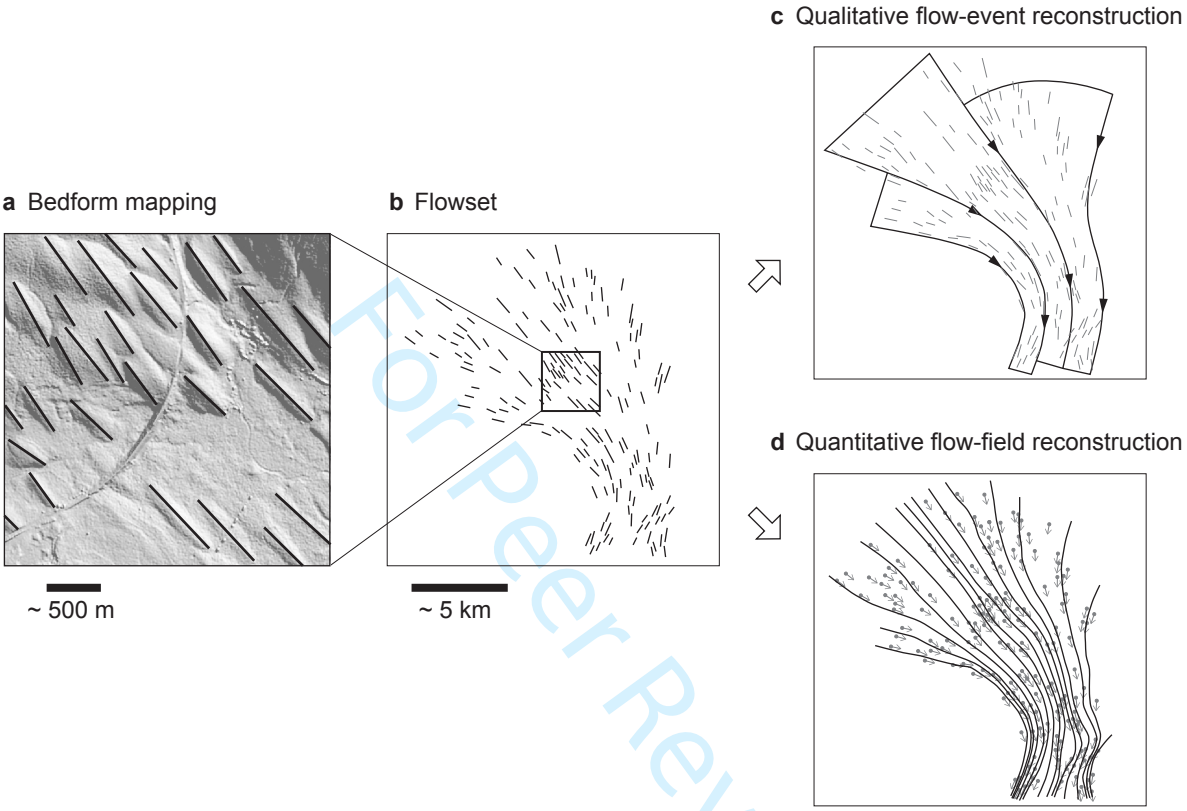

Figure 2

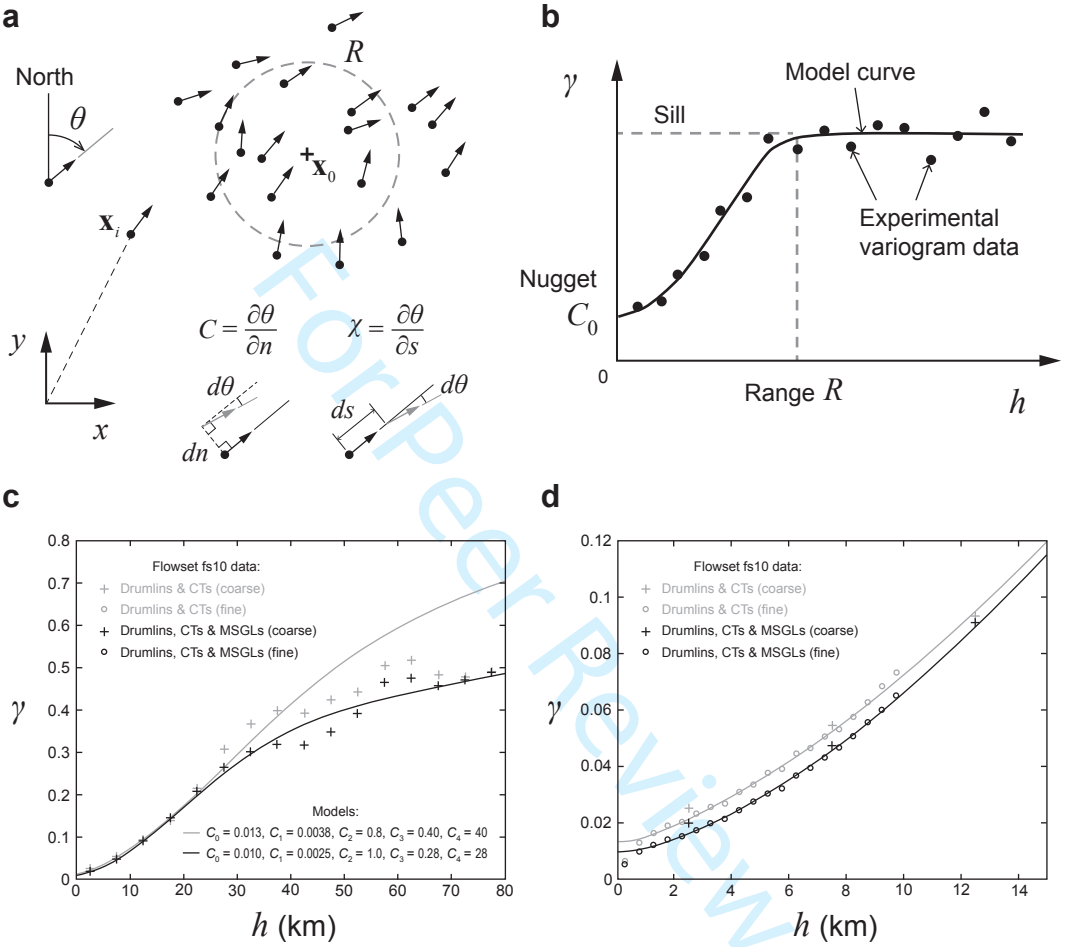

Figure 3

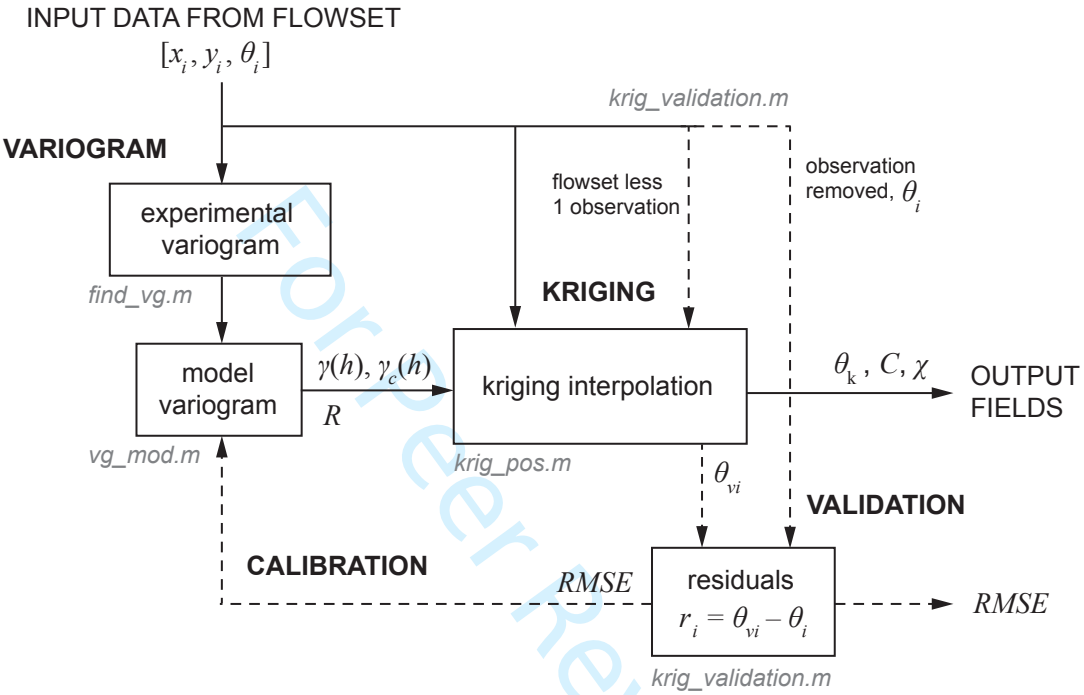

Figure 4

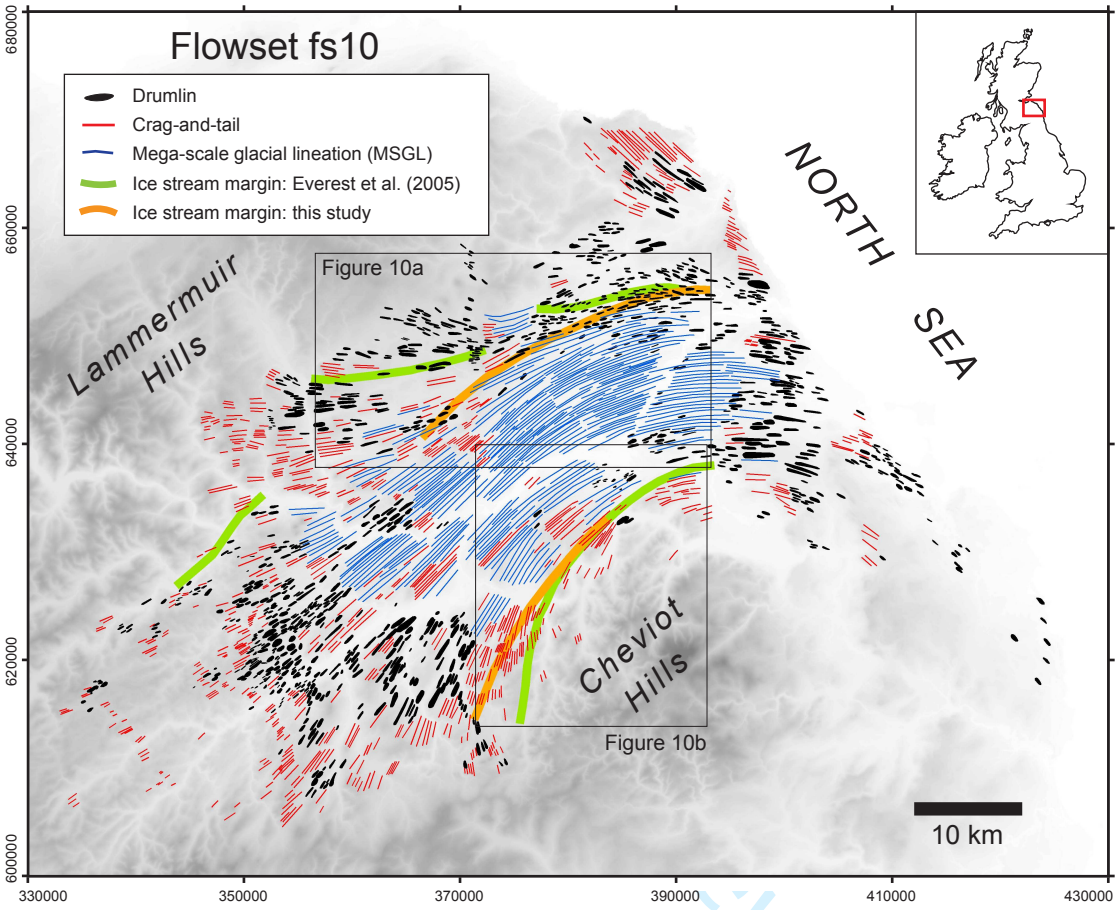
Flowset fs10
Drumlin
Crag-and-tail
Mega-scale glacial lineation (MSGL)
Ice stream margin: Everest et al. (2005)
Ice stream margin: this study
Figure 10a
Figure 10b
Lammermuir Hills
Cheviot Hills
NORTH SEA
10 km
680000
660000
640000
620000
600000
330000
350000
370000
390000
410000
430000

Figure 5

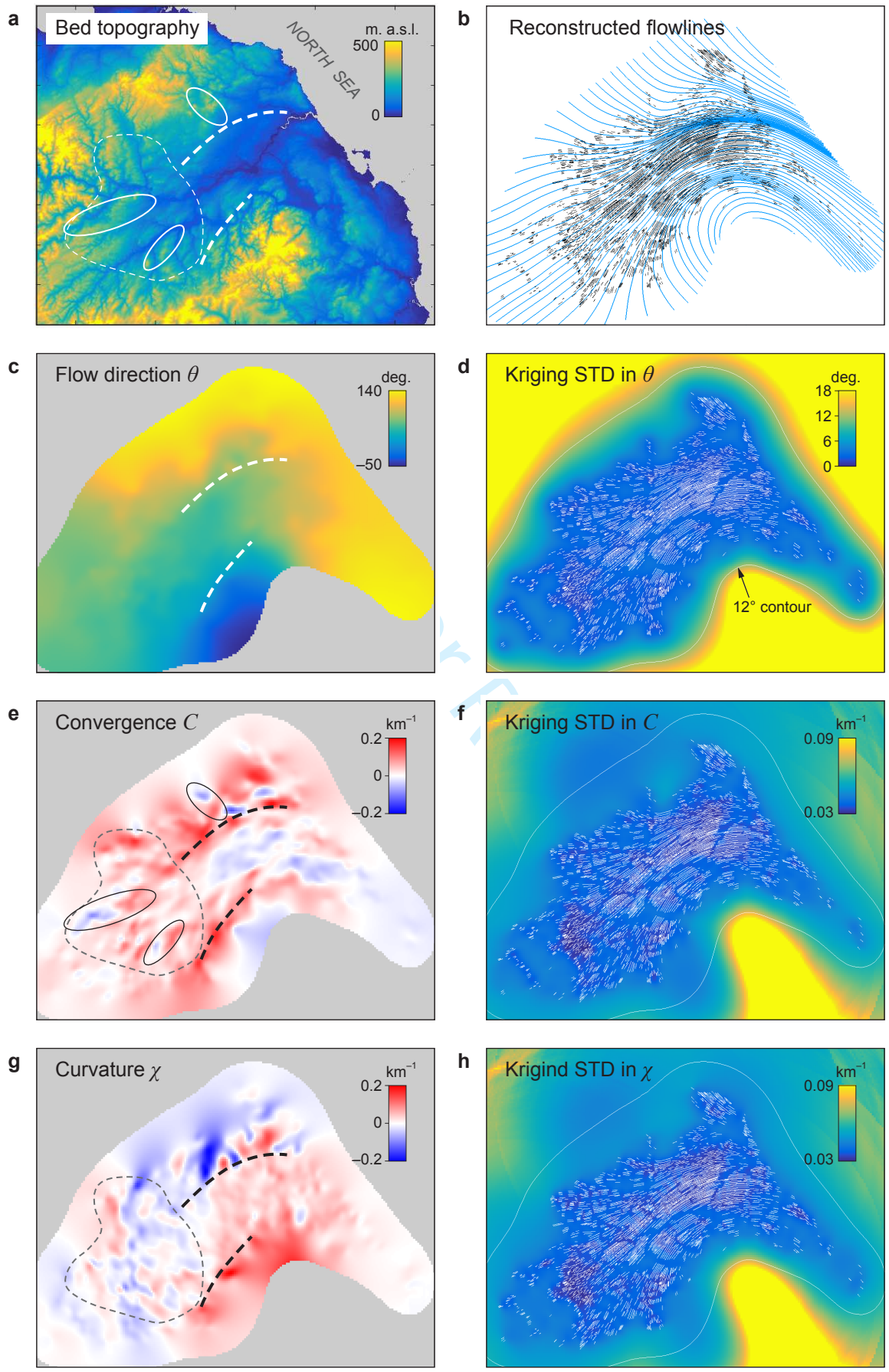
a
Bed topography
NORTH SEA
m. a.s.l.
500
0
b
Reconstructed flowlines
c
Flow direction θ
deg.
140
−50
d
Kriging STD in θ
deg.
18
12
6
0
12° contour
e
Convergence C
km⁻¹
0.2
0
−0.2
f
Kriging STD in C
km⁻¹
0.09
0.03
g
Curvature χ
km⁻¹
0.2
0
−0.2
h
Krigind STD in χ
km⁻¹
0.09
0.03

Figure 6

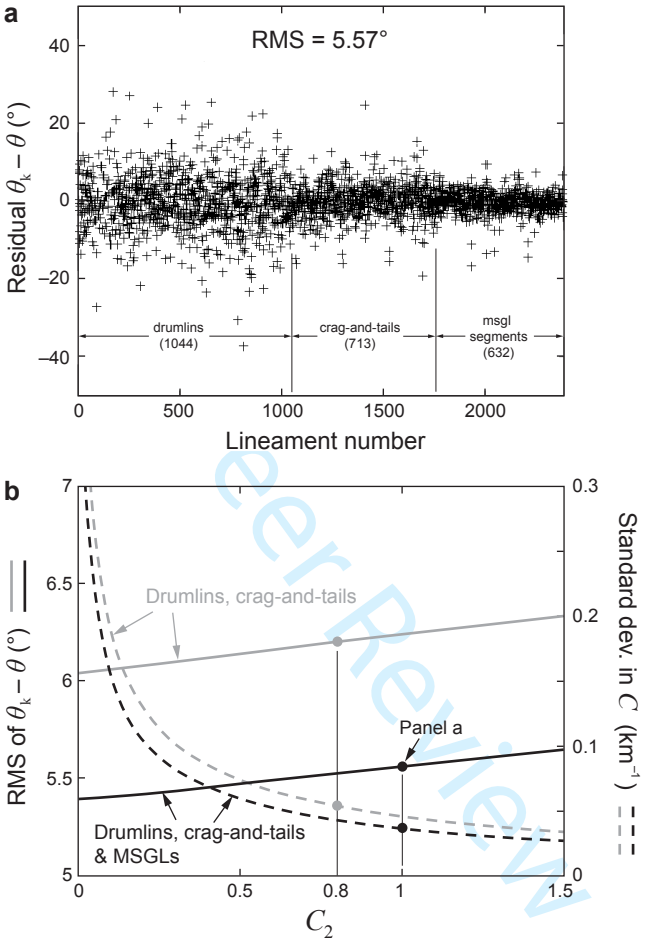

Figure 7

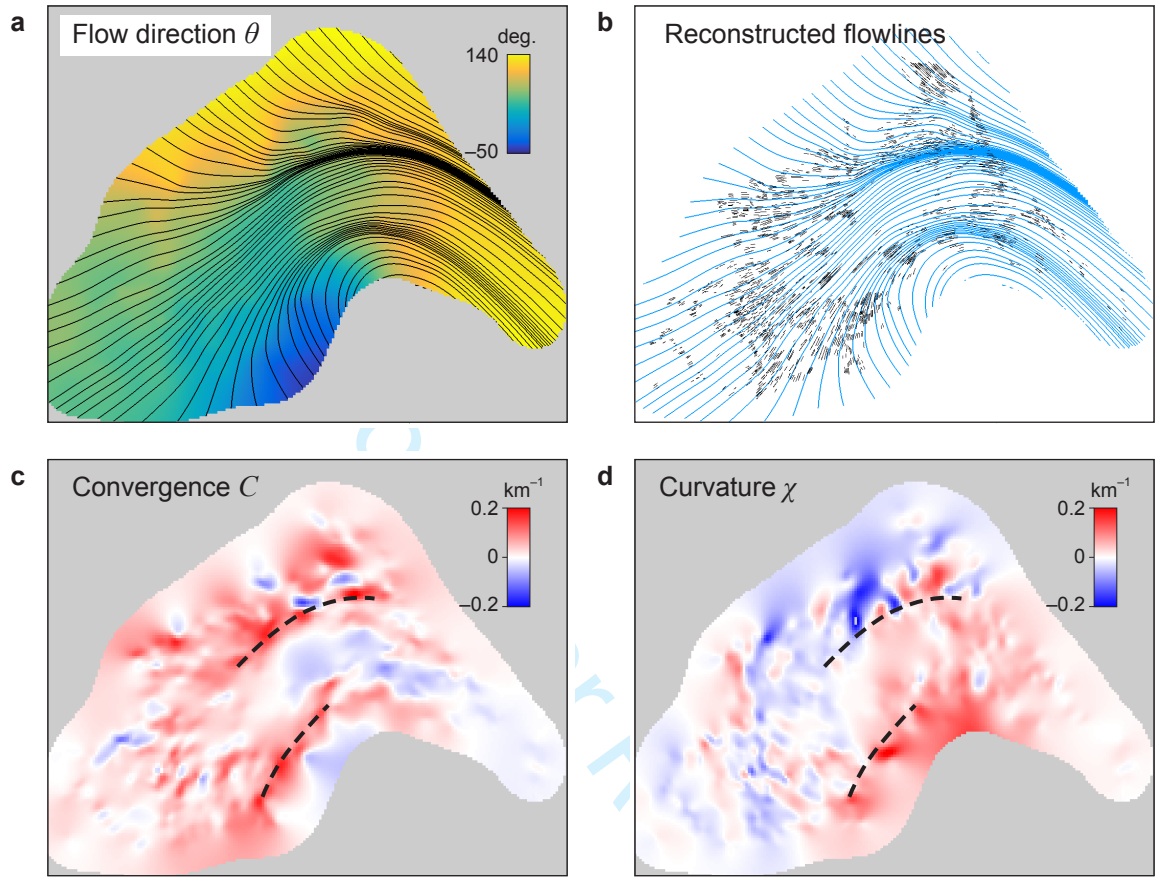
a
Flow direction θ
deg.
140
−50
b
Reconstructed flowlines
c
Convergence C
km⁻¹
0.2
0
−0.2
d
Curvature χ
km⁻¹
0.2
0
−0.2

Figure 8

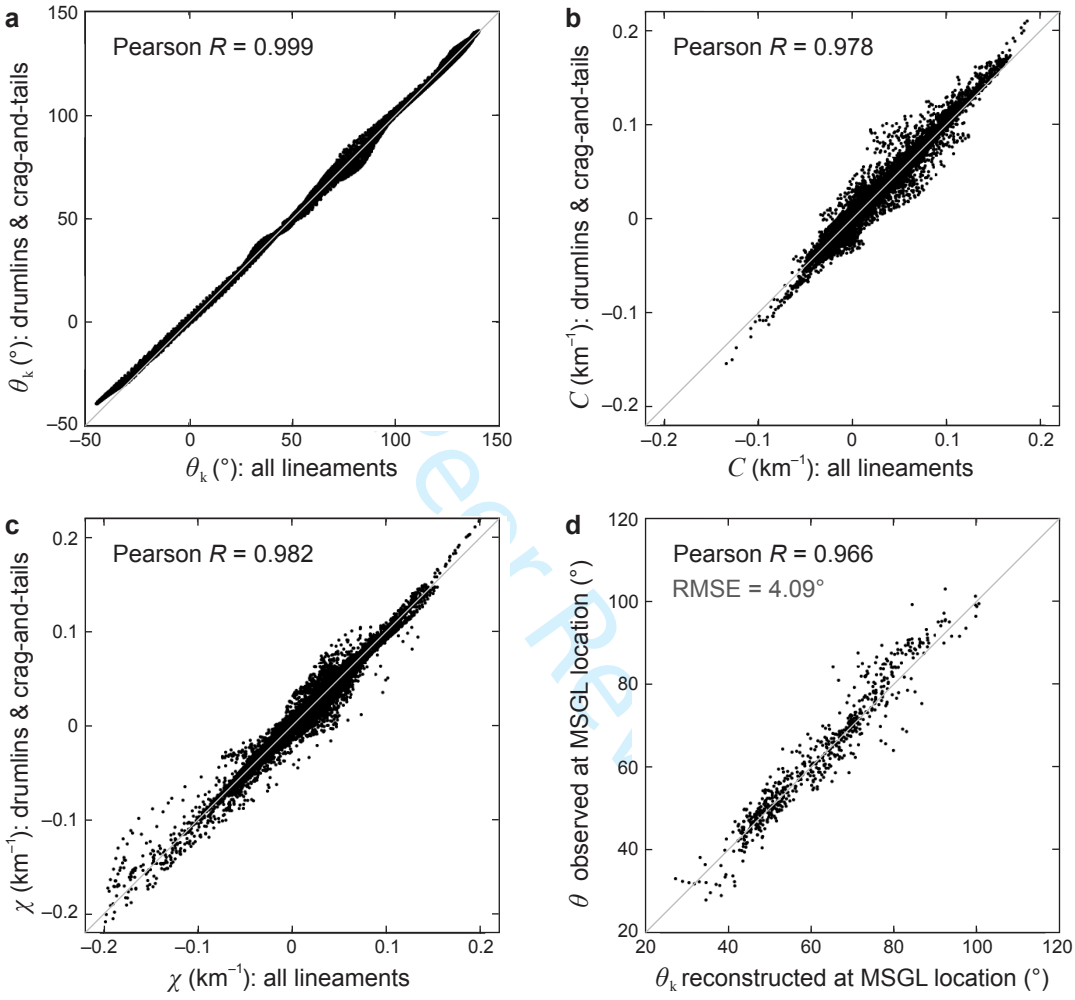
a
Pearson R = 0.999
θk (°): drumlins & crag-and-tails
θk (°): all lineaments
b
Pearson R = 0.978
C (km−1): drumlins & crag-and-tails
C (km−1): all lineaments
c
Pearson R = 0.982
χ (km−1): drumlins & crag-and-tails
χ (km−1): all lineaments
d
Pearson R = 0.966
RMSE = 4.09°
θ observed at MSGL location (°)
θk reconstructed at MSGL location (°)

Figure 9

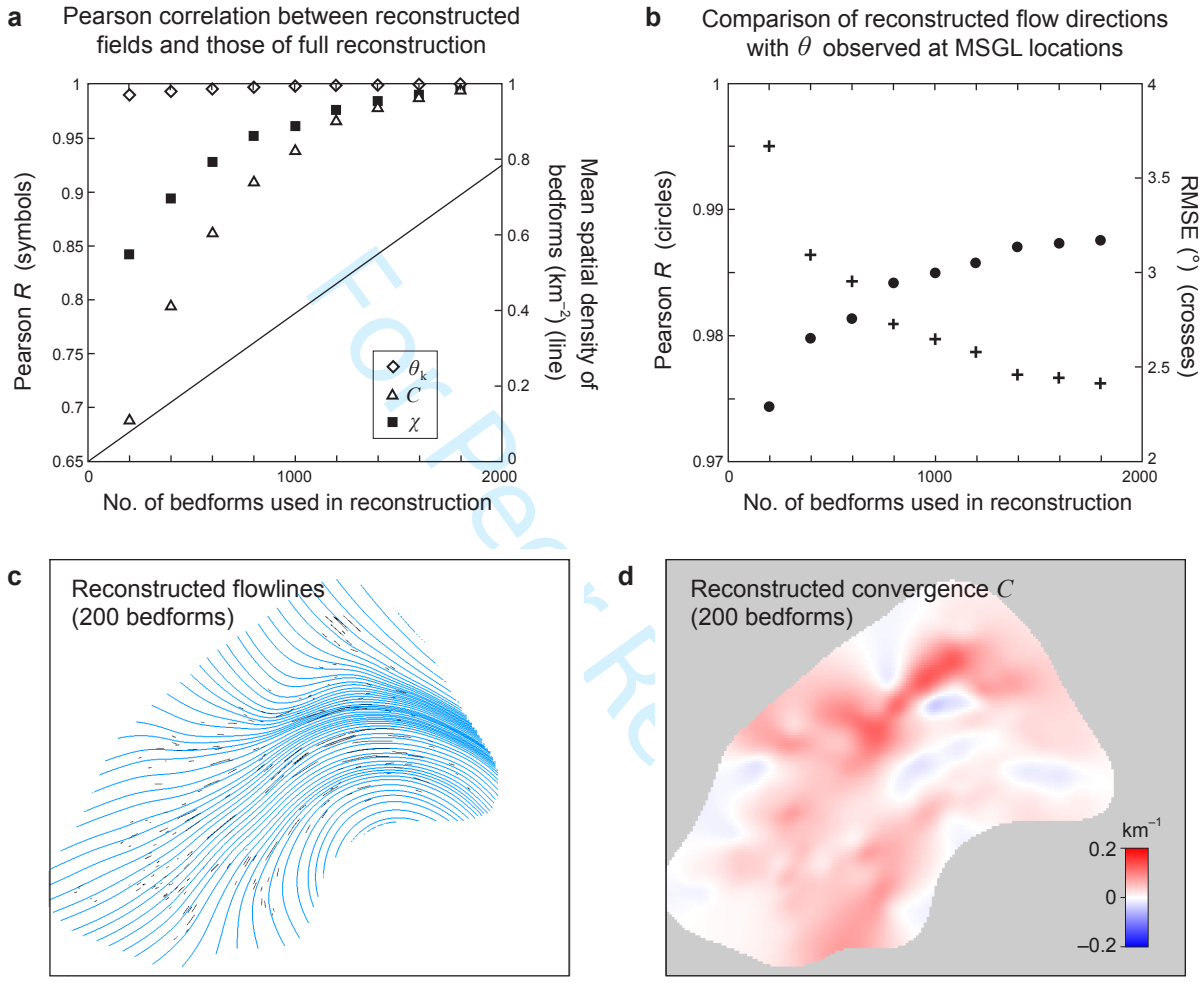
a
Pearson correlation between reconstructed fields and those of full reconstruction
Pearson R (symbols)
Mean spatial density of bedforms (km⁻²) (line)
No. of bedforms used in reconstruction
θk
C
χ
b
Comparison of reconstructed flow directions with θ observed at MSGL locations
Pearson R (circles)
RMSE (°) (crosses)
No. of bedforms used in reconstruction
c
Reconstructed flowlines (200 bedforms)
d
Reconstructed convergence C (200 bedforms)
km⁻¹
0.2
0
–0.2

Figure 10

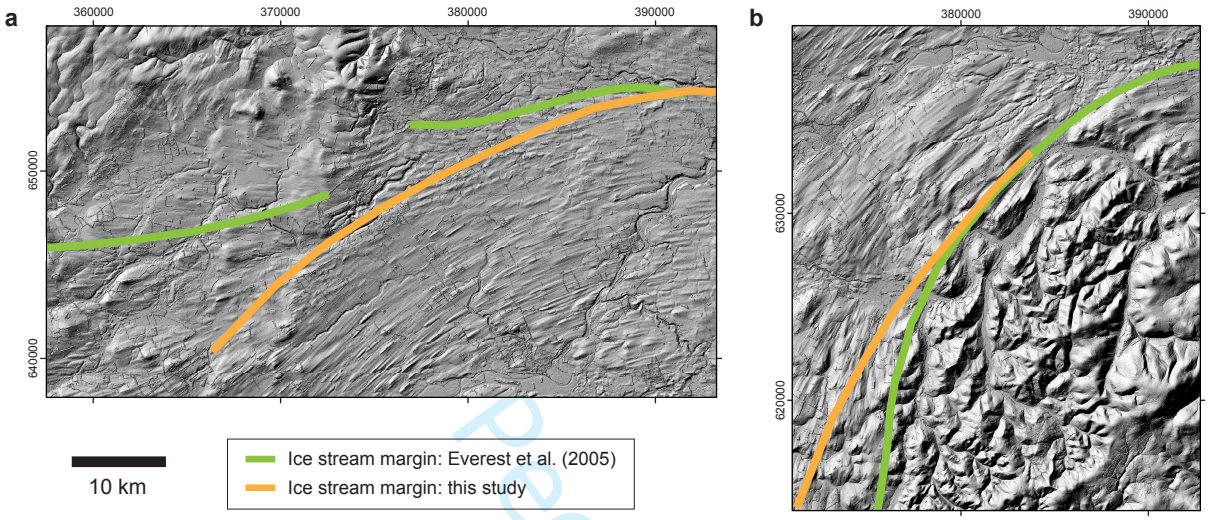

Graphical abstract

Reconstructing ice-flow fields from streamlined subglacial bedforms: a kriging approach

Felix S. L. Ng* and Anna L. C. Hughes
*Corresponding author

We present a quantitative method of reconstructing palaeo ice-flow fields from the flow directions measured from subglacial bedforms (such as drumlins, crag-and-tails, and mega-scale glacial lineations). Application of the method to bedforms of the Tweed Valley, UK, yields new glaciological information and insights about the Tweed palaeo-Ice Stream. MATLAB code of our toolset and data files of the case study are given at doi:10.15131/shef.data.6735131.